Manuscript prepared for Atmos. Chem. Phys.
with version 2015/09/17 7.94 Copernicus papers of the LaTeX class copernicus.cls.
Date: 27 November 2015

Understanding cirrus ice crystal number variability for different heterogeneous ice nucleation spectra

S. C. Sullivan[1], R. Morales Betancourt[2], D. Barahona[3], and A. Nenes[1,4,5]

[1]Department of Chemical and Biomolecular Engineering, Georgia Institute of Technology, Atlanta, GA 30332, USA
[2]Department of Civil and Environmental Engineering, University of Los Andes, Bogotá, Colombia
[3]NASA Goddard Space Flight Center, Greenbelt, MD 20771, USA
[4]Department of Earth and Atmospheric Sciences, Georgia Institute of Technology, Atlanta, GA 30332, USA
[5]ICE-HT, Foundation for Research and Technology, Hellas, 26504 Patras, Greece

Correspondence to: A. Nenes (athanasios.nenes@gatech.edu)

Abstract. Along with minimizing parameter uncertainty, understanding the cause of temporal and spatial variability of nucleated ice crystal number, N_i, is key to improving the representation of cirrus clouds in climate models. To this end, sensitivities of N_i to input variables like aerosol number and diameter provide valuable information about nucleation regime and efficiency for a given model formulation. Here we use the adjoint model of the Barahona and Nenes cirrus formation parameterization to understand N_i variability for various ice-nucleating particle (INP) spectra. Inputs are generated with the Community Atmosphere Model version 5, and simulations are done with a theoretically-derived spectrum, an empirical lab-based spectrum, and two field-based empirical spectra that differ in the nucleation threshold for black carbon particles and in the active site density for dust. The magnitude and sign of N_i sensitivity to insoluble aerosol number can be directly linked to nucleation regime and efficiency of various INP. The lab-based spectrum calculates much higher INP efficiencies than field-based ones, which reveals a disparity in aerosol surface properties. N_i sensitivity to temperature tends to be low, due to the compensating effects of temperature on INP spectrum parameters; this low temperature sensitivity regime has been experimentally reported before but never deconstructed as done here.

1 Introduction

Aerosol-cloud interactions remain the largest source of uncertainty in projections of anthropogenic climate change, and aerosol-ice interactions, in particular, are poorly understood [Boucher et al. 2013]. Atmospheric aerosol may modulate the properties of pure ice clouds by providing particles upon which new ice crystals form. Cirrus clouds control moisture transfer into the lower stratosphere and can have a net warming effect [e.g., Chen et al. 2000; Brewer 1949; Jensen et al. 1994].

Ice crystals within cirrus clouds can be formed in a variety of ways. Heterogeneous nucleation refers to the formation of ice on an aerosol surface, and the portion of aerosol upon which ice forms this way are called ice-nucleating particles (INP). There are several modes of heterogeneous freezing: in deposition nucleation, vapor deposits directly onto an aerosol; in condensation freezing, the aerosol acts first as a cloud condensation nucleus and then immediately as an INP; and in immersion freezing, an aerosol submerged for some time in supercooled liquid eventually initiates ice formation. Ice crystals may also form directly from an aqueous phase through homogeneous nucleation, typically at temperatures below about 235 K [Pruppacher and Klett 1997]. Aircraft measurements of relative humidity and ice crystal number concentrations indicate that heterogeneous nucleation is dominant for synoptic cirrus over North and Central America [Cziczo et al. (2013)]. But both mechanisms can be active in cirrus clouds, and the competition for water vapor between homogeneous and heterogeneous ice nucleation must be included in cirrus formation parameterizations [Barahona and Nenes 2008, 2009a, b; Lin et al. 2005].

Much effort has been devoted to studying heterogeneous ice nucleation on a fundamental level [e.g., Reinhardt and Doye 2014; Lupi et al. 2014; Cox et al. 2015]. Ice nucleation can be understood as the formation of an ice germ in the vicinity of an active site. The nature of active sites is unknown, but current understanding suggests that they promote ordering of the water molecule layers near the particle surface. The active site density refers to the number of these sites per unit of aerosol surface area. A particle with more surface area will tend to have more active sites and nucleate at higher temperatures (or lower supersaturations); however, each active site varies in its efficiency, so that contact angle or site density distributions are necessary [Barahona 2012; Kulkarni et al. 2012].

While Köhler theory is the accepted framework to describe droplet activation, nothing analogous exists for ice. Two conceptual paradigms are currently in use: stochastic and singular freezing [Pruppacher and Klett 1997; Vali 2014]. In the stochastic paradigm, water molecules fluctuate randomly to and from a particle surface with some probability of reaching a critical, stable germ size that initiates formation of the new phase; homogeneous nucleation within a supercooled droplet is understood this way. In the singular paradigm, nucleation is determined solely by particle surface morphology; once a characteristic threshold temperature or supersaturation is acquired, ice nucleates.

Parameterizations of heterogeneous ice nucleation calculate the heterogeneously-formed ice crystal number, $N_{i,het}$, as a function of thermodynamic conditions and precursor aerosol properties. These parameterizations, termed INP spectra hereafter, may be empirically or theoretically based. Empirical spectra use lab or field data to calculate an active site density. Theoretically based spectra use classical nucleation theory and calculate a nucleation rate proportional to the aerosol surface area [e.g., Karcher and Lohmann 2002; Liu and Penner 2005; Niemand et al. 2012; Barahona and Nenes 2009b; Marcolli et al. 2007]. The surface heterogeneity should also be considered and has recently been represented as a distribution of contact angles [Savre et al. 2013; Wang et al. 2014]. But ice nucleation data is geographically- or thermodynamically-limited, taken only in localized regions or

over a narrow range of temperatures and pressures. And classical nucleation theory is approximate and requires unknown or variable surface property data. As a result, the output of INP spectra has remained uncertain, with up to three orders of magnitude difference in calculated N_i [e.g., Barahona et al. 2010].

Early published INP spectra expressed active site density as a function of only temperature or supersaturation and neglected the aerosol composition and size. For example, Fletcher 1969 proposed a parameterization based solely on temperature, valid down to about -25°C. The Meyers et al. INP spectrum describes deposition and condensation nucleation as a function of supersaturation only, with data from a continuous-flow diffusion chamber [Meyers et al. 1992]. They observed a logarithmic increase in the number of ice-nucleating aerosol with supersaturation with respect to ice, s_i.

More recently published INP spectra consider the effects of size distribution and composition of ice-nucleating particles. For example, Phillips et al. 2008 (PDA08) calculates the active site density for mineral dust, black carbon, and hydrophobic organics, constrained with data from the First and Second Ice Nuclei Spectroscopy Studies (INSPECT-1 and -2) and the Cirrus Regional Study of Tropical Anvils and Cirrus Layers - Florida-Area Cirrus Experiment (CRYSTAL-FACE) [Phillips et al. 2008]. Updates have been made in the Phillips et al. 2013 spectrum (PDA13). PDA08 and PDA13 are based on the singular paradigm, in which each aerosol type nucleates ice at threshold temperatures and supersaturations. Several other studies have parameterized nucleation efficiency of mineral dusts or illite powders, using cloud chamber data or optical microscopy [e.g., Connolly et al. 2009; Niedermeier et al. 2010; Broadley et al. 2012; Niemand et al. 2012]. Hiranuma et al. have also developed an INP spectrum at cirrus-relevant temperatures, using the Aerosol Interaction and Dynamics in the Atmosphere (AIDA) cloud chamber data for hematite particles [Hiranuma et al. 2014]. This study uses the three aforementioned spectra to describe deposition nucleation. Other empirical spectra and recent heterogeneous ice nucleation experiments are further discussed in the review by Hoose and Möhler 2012.

Numerous studies have examined the impact of INP spectrum on nucleated ice crystal number. Using the NCAR Community Atmosphere Model (CAM), Xie et al. evaluated how predicted cloud type, cloud properties, and radiative balance change based on the INP spectrum [Xie et al. 2013]. The study uses Meyers et al. 1992 as a default spectrum compared to DeMott et al. 2010, a spectrum which links N_i with the aerosol number of diameter larger than 0.5 μm. DeMott et al. calculated a much lower N_i, and hence a higher liquid water path and lower ice water path for Arctic mixed-phase clouds. Curry and Khvorostyanov have also run Meyers et al. 1992, DeMott et al. 1998, Phillips et al. 2008, and their own theoretical INP spectra with parcel model simulations over a range of thermodynamic conditions [Curry and Khvorostyanov 2012]. The authors emphasize the importance of applying empirical spectra only in their regions of validity and note that low nucleating efficiencies in PDA08 may underestimate ice crystal number. Prenni et al. noted that Meyers et al. significantly

overpredicted ice water content in coupled models if aerosol were not depleted after nucleation [Prenni et al. 2007]. When INP depletion was included, the predictions of water and ice in mixed-phase clouds improved considerably. Barahona et al. compared the output crystal number between PDA08, Meyers et al., Murray et al. 2010, and the Barahona and Nenes CNT spectrum for both monodisperse and polydisperse aerosol [Barahona et al. 2010]. They found that ice nucleation occurred more often in the competitive regime for the Meyers et al. spectrum, yielding smaller crystal numbers; however, PDA08 predicted higher crystal numbers with ice nucleation most frequently in the homogeneous regime. Similar results have also been reported for mixed-phase cloud conditions [e.g., Morales-Betancourt et al. 2012].

In this work, we extend the adjoint of a cirrus formation parameterization [Sheyko et al. 2015] to perform sensitivity analysis for several heterogeneous INP spectra. Adjoints can calculate the sensitivity of a given output to all inputs more efficiently and accurately than finite difference runs, but at the expense of code development [Errico 1997; Giering and Kaminski 1998]. Karydis et al. have constructed the adjoint model of a liquid droplet parameterization, and others have used adjoints for data assimilation, for example in the Community Multiscale Air Quality and ISORROPIA models [Hakami et al. 2007; Karydis et al. 2012; Capps et al. 2012]. Here we use the adjoint approach to address the following: how and why N_i and its sensitivities change with the INP spectrum used and how sensitivities can elucidate nucleation regime and efficiency. Our focus is on spatial and temporal output variability, distinct from output uncertainty. The development of heterogeneous ice nucleation spectra reduces parameter uncertainty; once a spectrum is chosen, the question of how input variables contribute to output variability remains. We consider the latter here. Section 2 provides an overview of the nucleation parameterization, model inputs, and four INP spectra used. Crystal number fields and aerosol acting as INP are presented in sections 3.1 and 3.2. Sensitivities of different spectra are discussed in sections 3.3 to 3.6, and section 4 summarizes the work.

2 Methods

2.1 BN parameterization

We use the Barahona and Nenes cirrus formation parameterization (BN09) [Barahona and Nenes 2008, 2009a, b] and its adjoint [Sheyko et al. 2015]. BN09 describes the competition for water vapor between heterogeneous and homogeneous nucleation; the number of heterogeneously-formed crystals, $N_{i,het}$, is calculated from any of a variety of nucleation spectra, and homogeneously-formed number, $N_{i,hom}$, is calculated with an approximate solution to the coupled mass and energy balances of a cirrus cloud parcel. Then the total ice crystal number, N_i, is the sum of the heterogeneous and homogeneous contributions (Equation 1). When the temperature is greater than about -38°C, homogeneous nucleation ceases because it is kinetically unfavorable. Homogeneous nucleation is also suppressed when the number of INP exceeds a certain threshold, N_{lim}, and the maximum super-

saturation that develops within the cloud parcel, s_{max}, is less than the threshold for homogeneous nucleation, s_{hom}. In this case, s_{max} must be numerically calculated from the growth and supersaturation evolution equations.

$$N_i = \begin{cases} N_{i,hom} + N_{i,het}(s_{hom}), & N_{i,het}(s_{hom}) < N_{lim} \\ N_{i,het}(s_{max}), & N_{i,het}(s_{hom}) \geq N_{lim} \end{cases} \quad (1)$$

The BN parameterization make two principal assumptions: first, ice crystal growth occurs mostly in the free growth regime where new nucleation does not significantly change the parcel supersaturation, and second, N_i is calculated at the maximum supersaturation rather than a supersaturation later in the freezing pulse. These assumptions lead to overestimation of N_i at lower temperatures and higher updraft velocities and underestimation of N_i at lower updrafts, when the freezing pulse is longer. For a wide range of cirrus formation conditions, however, the parameterization output matches that of a detailed parcel model to within 5%. These points are discussed in Barahona and Nenes 2008.

As in Sheyko et al., the TAPENADE automatic differentiation tool was used to create an adjoint model of BN09 (ABN15 hereafter) [Hascoët and Pascual 2004]. For the finite series of operations that link N_i to the inputs in BN09, TAPENADE uses the chain rule to propagate a perturbation in the output, dN_i, back to differentials in the input variables. Once developed, the adjoint model saves significant computational time, relative to a finite difference method, and avoids both approximation and truncation errors. ABN15 differentiates N_i with respect to 13 input variables: temperature; updraft velocity; accumulation and coarse mode dust numbers and diameters; organic aerosol number and diameter; black carbon number and diameter; sulfate number and diameter; and water vapor deposition coefficient. All derivatives, along with the typical output of BN09, are evaluated at the input model state for each grid cell and time step of a GCM run. ABN15 is verified with centered finite difference approximations, using perturbations of $\pm$ 0.1% around each input for simulation-relevant thermodynamic and aerosol conditions. Such finite difference calculations require two runs for each variable, so for 13 input variables, the adjoint model saves 25 executions of the parameterization relative to typical sensitivity calculations.

2.2 Simulation setup and spectra

Simulation inputs are generated from the NCAR Community Atmosphere Model, version 5 (CAM5) at the 232 hPa pressure level with two year spin-up and 2.5 x 1.88° resolution. The input updraft velocity from CAM 5.1 is calculated from the turbulent kinetic energy in the moist turbulence scheme of Bretherton and Park 2009 as w_{sub} = $\sqrt{\frac{2}{3}\mathrm{TKE}}$. The probability distribution of these values is compared to two years' worth of millimeter cloud radar measurements in Figures 8 and 9 with all values at the same latitude, longitude, and altitude. Measurements are shown after Doppler velocity

decomposition, as described in Kalesse and Kollias 2013. Shi et al. have also looked at distributions of input updraft velocity for CAM simulations of ice nucleation,

Muhlbauer et al. compared the measured updraft distributions from both aircraft and ground-based MMCR and saw some underestimate.

The distribution of hourly-averaged measurements has a lower maximum and decays to smaller values than that of the hourly-averaged simulation inputs. We use daily-averaged values for which the distribution agrees better with the observed values. w_{sub} values from CAM are used as the standard deviation $\sigma_{sub,w}$ of a Gaussian updraft velocity distribution $P(w)$ of mean $\mu_{sub,w}$ = 0.1 cm s^{-1}. Both output ice crystal numbers and sensitivities are weighted over this distribution to account for sub-grid variability [Guo et al. 2008; Betancourt and Nenes 2010]:

$$\overline{f(w)} = \frac{\int_0^\infty f(w)P(w)dw}{\int_0^\infty P(w)dw}. \tag{2}$$

This integration is performed numerically with a six-point Legendre-Gauss quadrature method, with weights and abscissae chosen over an interval from minimum to maximum velocity which are taken as four standard deviations below and above $\mu_{sub,w}$. An upper bound of 3 m s^{-1}, unlike that of 0.2 m s^{-1} used in Zhang et al. 2013 and Shi et al. 2015, and a lower bound of 0.001 m s^{-1} are enforced.

The altitude examined is in the middle of the ISCCP cloud classification for cirrus (pressures between 440 and 50 hPa) and represents pure ice cloud formation. The Lamarque et al. emissions inventory [Lamarque et al. 2010] and MAM3 module were used [Liu et al. 2012a]. Lognormal size distributions are assumed for all aerosol types with geometric standard deviations, σ_g, assumed constant and listed below in Table 1. σ_g and total aerosol mass are used to determine geometric mean diameter for each mode. Total aerosol number is scaled by mass fraction to determine aerosol number concentrations in each mode [Morales-Betancourt and Nenes 2014]. For calculations of ice crystal number concentrations and sensitivities, BN09 and ABN15 were run over a year with four heterogeneous INP spectra and daily-averaged values of CAM output.

2.3 Phillips et al. empirical spectra

PDA08 uses the exponential correlation of crystal number and supersaturation in Meyers et al. as a reference spectrum, extending the applicable ranges of temperature and supersaturation and incorporating characteristics of the precursor aerosol. The number of ice-nucleating particles, $n_{INP,X}$ in aerosol group X (dust and metallics - DM, black carbon - BC, or organics - O) is calculated with a sum over the aerosol size distribution weighted by a freezing fraction:

$$n_{INP,X} = \int_{\log 0.1\mu m}^{\infty} \{1 - \exp[-\mu_X(D, S_i, T)]\}\, n_X(\log D)\, d\log D \tag{3}$$

μ_X represents the number of ice embryos forming per aerosol and is the product of the active site density and aerosol surface area [Steinke et al. 2014]: $\mu_X = H_X(S_i,T)\xi(T)\left(\frac{\alpha_X\, n_{INP,*}}{\Omega_{X,*}}\right)\pi D^2$. $n_{INP,*}$ is the INP number from a reference activity spectrum; $\Omega_{X,*}$ is a reference aerosol surface area, which acts as a normalization factor for the size distribution; α_X is the portion of aerosol number belonging to group X within $n_{INP,*}$; $n_X(\log D)$ is the aerosol size distribution; and H_X is a threshold function that reduces INP concentrations at conditions subsaturated with respect to water and warm sub-zero temperatures in agreement with observations. H_X equals unity at water saturation and steps at certain threshold temperatures, $T_{0,X}$, and supersaturations, $s_{i,0,X}$, for the different aerosol groups. Finally $\xi(T)$ diminishes heterogeneous nucleation at warm sub-zero temperatures.

Both PDA08 and PDA13 adopt the mathematical framework of Equation 3, but PDA13 employs more extensive field campaign data [Phillips et al. 2013]. The organic classification in PDA13 is also split into primary biological material and glassy organics, following recent observations of distinct ice-nucleating activity for these particle types. In this study, sensitivity of N_i to biological INP is not considered, as CAM5 does not currently output a biological particle number.

2.4 Classical nucleation theory spectrum

We also use the classical nucleation spectrum developed by Barahona and Nenes and presented in conjunction with the parameterization [Barahona and Nenes 2009b]:

$$n_{INP,X} = e_X n_X(\log D)\min\left[\frac{s_i}{s_{i,0,X}} e^{-f(\cos\theta)\, k_{hom}\, (s_{i,0,X} - s_i)}, 1\right] \tag{4}$$

where e_X is the nucleation efficiency of aerosol group X, $s_{i,0,X}$ is the threshold supersaturation, $n_X(\log D)$ is the aerosol size distribution, θ is the INP-ice contact angle, and k_{hom} is a parameter related to the homogeneous nucleation threshold. Dust and black carbon groups are included with parameters listed in Table 1; contact angles come from the laboratory data of Chen et al. 2008 and e_{DM} is similar to that in Möhler et al. 2006. The stochastic component of the nucleation efficiency through heterogeneous nucleation rate coefficient is assumed negligible, and the singular paradigm also underlies this spectrum. e_X is potentially a function of temperature and the aerosol profile, but here it is taken from literature and assumed constant throughout the simulation.

2.5 Hiranuma et al. spectrum

The nucleation efficiency of hematite particles was measured at the AIDA chamber from -78°C up to -36°C and parameterized [Hiranuma et al. 2014]. The third-order polynomial fit for active site density (in m^{-2}) is given in Equation 5 as a function of temperature and saturation ratio of ice. Isolines from AIDA expansion cooling experiments are interpolated over the temperature-supersaturation

space, assuming a hematite baseline surface area of 6.3×10^{-10} $\mathrm{m^2L^{-1}}$.

$$n_s(T,S_i) = -3.777\times10^{13} - 7.818\times10^{1}1T + 4.252\times10^{13}S_i - 4.598\times10^{9}T^2 + 6.952\times10^{11}T\cdot S_i - 1.111\times10^{13}S_i^2 - 2.966\times10^{6}T^3 + 2.135\times10^{9}T^2\cdot S_i - 1.729\times10^{4}T\cdot S_i^2 - 9.438\times10^{11}S_i^3 \quad (5)$$

As in Hiranuma et al. 2014, we use this active site parameterization in the framework of Equation 3 to calculate nucleated crystal number:

$$n_{INP,X} = \int_{\log 0.1\mu m}^{\infty} \{1-\exp[-n_s(T,S_i)\pi D^2]\}\, n_X(\log D)\, d\log D. \quad (6)$$

Hereafter, we refer to this formulation as the AIDA spectrum.

3 Results

Homogeneous and heterogeneous nucleation can be active in cirrus clouds, and their relative influence can be conceptually understood along an INP-N_i trace shown in Figure 1a [Ren and MacKenzie 2005; Barahona and Nenes 2009a]. When INP concentration is low, nucleation is predominantly homogeneous. The slope or sensitivity here, $\partial N_i/\partial N_{\mathrm{INP}}$, is slightly negative because the addition of an insoluble particle slightly decreases the number of nucleated ice crystals by competing for water vapor and decreasing supersaturation. As the INP concentration increases, homogeneous and heterogeneous nucleation compete more strongly for water vapor. Water vapor preferentially deposits on the additional INP surface and depresses the number of newly-nucleated crystals, so $\partial N_i/\partial N_{\mathrm{INP}}$ increases in magnitude. Eventually, INP increases beyond the threshold number, N_{lim}, and further depletion of supersaturation inhibits homogeneous nucleation altogether. Addition of another INP increases the ice crystal number, and $\partial N_i/\partial N_{\mathrm{INP}}$ becomes positive. While all nucleation for $N_{INP} < N_{lim}$ is competitive, we use the term 'competitive nucleation' below to refer to the case when both homogeneous and heterogeneous nucleation have a significant contribution, greater than 10%, to N_i. These three regimes have been explained in terms of INP number, but they can also be understood in terms of INP diameter: increasing INP surface area leads to more vapor depletion by heterogeneous nucleation and decreased crystal number in the competitive regime.

This conceptual framework is used to understand the simulation results.

3.1 Crystal number

Figure 3 shows a comparison of the in-situ crystal number measurements, taken from the NASA MACPEX (Mid-latitude Cirrus Properties Experiment) and the DOE SPARTICUS (Small Particles In Cirrus) aircraft campaigns. Data are used from the Video Ice Particle Sampler (VIPS) and Two-Dimensional Stereo (2DS) probe during April 2011 of MACPEX and from the Forward Scattering

Spectrometeor Probe (FSSP) during January 2010 of SPARTICUS. Using simultaneous Meteorological Measurement System (MMS) pressure values, only N_i measurements taken within 20 hPa of the simulated pressure level of 232 hPa are used. Because the newly-nucleated ice crystal number concentration is simulated, we use only N_i from the smallest size bins of each instrument (see caption of Fig. 3). Finally, the same criterion for significant samples as in Jensen et al. 2013 is employed: samples must continuously span at least 45 s. These MACPEX and SPARTICUS measurements, taken with shatter-resistant probes and analyzed with an inter-arrival time algorithm, are more reliable than older ones, especially for the smallest size bins that we consider [Jensen et al. 2013].

Simulated and measured N_i agree best for the PDA13 spectrum, followed by the PDA08 and then the AIDA spectra. The CNT spectrum overestimates the frequencies of N_i greater than about 10 L^{-1} by more than an order of magnitude and predicts no number concentrations less than 1 L^{-1}. Measurements show, instead, that most of the smallest crystals occur at lower number concentrations, below about 5 L^{-1}. The very high frequency of low N_i is missed by the other spectra as well, and all except PDA13 show slower decays in the frequency of high N_i than those in the measurements.

Model overestimate of high N_i at the coldest temperatures has been often noted [e.g., Krämer et al. 2009; Jensen et al. 2010; Barahona and Nenes 2011]. Along with this “ice nucleation puzzle" of low N_i at low temperature [Spichtinger and Krämer 2013], model-measurement discrepancy may be explained by in-cloud processes after nucleation: nucleated crystal number will tend to be higher than in-cloud crystal number, even when looking only at the smallest size bins. Preexisting ice crystals can inhibit ice nucleation [Barahona and Nenes 2011; Shi et al. 2015], while sedimentation can significantly reduce N_i. Spichtinger and Gierens 2009 have termed the latter “sedimentation induced quenching of nucleation", and Jensen et al. 2013 found that omission of sedimentation by setting crystal fall speed to 0 m s^{-1} resulted in higher frequency of N_i greater than 1000 L^{-1}.

Figures 2a through d show the annually-averaged potential nucleated ice crystal number for each grid cell, given the vertical velocity and aerosol profile. The spatial variability in these fields is notable and reflects the large, documented spatial variability in INP concentrations [e.g., DeMott et al. 2010; Murary et al. 2012]. Including additional microphysics after nucleation will tend to reduce this spatial variability. Some common features are still observed between fields: over the Himalayas and Rockies, N_i is higher because orographic lifting generates stronger updrafts and more supersaturation; the Saharan and Gobi desert outflows enhance $N_{i,het}$; and for INP spectra considering black carbon (all except the AIDA spectrum), higher $N_{i,het}$ occurs in regions of biomass burning (e.g., sub-Saharan Africa and the Amazon). In the Southern Hemisphere, especially over Antarctica, heterogeneous nucleation is rare and N_i stays high because aerosol number concentrations are low and active site density decreases with temperature.

Elsewhere, N_i is highly variable and sensitive to the INP spectrum. For example, all spectra except PDA08 see higher crystal number in the Northern than the Southern Hemisphere. In agreement with previous studies, PDA08 predicts the lowest INP number, between 0.047 and 5.07 L^{-1}, (Table 2)

and the highest maximum supersaturations [Barahona et al. 2010; Curry and Khvorostyanov 2012; Morales-Betancourt et al. 2012]. When the input aerosol number is sufficiently high in the Northern Hemisphere, stronger competitive nucleation results in lower N_i, while the Southern Hemisphere remains dominated by homogeneous nucleation and higher N_i. The heterogeneously-formed fraction field in Figure 10 also illustrates these regions of competitive and homogeneous nucleation in the NH and SH respectively. Updraft velocity and N_i are well-correlated; both have higher values around the equator for PDA08.

Compared to PDA08, PDA13 predicts about an order of magnitude higher INP number, between 0.57 and 28.6 L^{-1} and more frequent inhibition of homogeneous nucleation, as shown in Figure 10, where the heterogeneously-formed fraction of N_i is much higher. In localized regions of purely heterogeneous nucleation, however, PDA08 may still predict higher N_i. This can be understood in terms of an INP abundance, $A_{\mathrm{INP}} \equiv N_{INP}/N_{lim}$, defined as the ratio of available INP to the limiting number to inhibit homogeneous nucleation. N_{lim} increases with decreasing maximum supersaturation, $N_{lim} \propto S_{i,max}/(S_{i,max}-1)$, and this increase in N_{lim} can outweigh the increase in INP number so that A_{INP} actually decreases within PDA13.

Higher N_i in PDA08 can also be understood in terms of threshold supersaturations for nucleation, when calculated supersaturations are similar between PDA08 and PDA13. When these thresholds are less stringent, the competitive nucleation cusp of the INP-N_i trace becomes steeper and extends to lower N_i values. Where nucleation is competitive, then, as in PDA13 around the equator, very low N_i is possible.

Compared to PDA13, INP numbers in the CNT and AIDA spectra are about tenfold higher, with median values of 50.38 and 52.51 L^{-1} respectively. High INP numbers result in almost purely heterogeneous nucleation everywhere for the CNT spectrum, as shown in Figure 10c. The highest crystal numbers in any of the fields occur for this spectrum in Saharan outflows because of the high dust nucleation efficiency and the dependence on aerosol number concentration rather than surface area here. Large accumulation mode dust numbers can yield large A_{INP}. N_i is on the order of 1000 L^{-1} here, larger than any of the in-situ measurements shown in Figure 3. An overestimate of INP by CNT-based spectra has been reported elsewhere [e.g., Liu et al. 2012b].

For the AIDA spectrum, mostly heterogeneous nucleation occurs in the Northern Hemisphere, while competitive nucleation occurs in the Southern Hemisphere. INP increases lead to frequent inhibition of homogeneous ice nucleation for these last two spectra. Again, higher N_i are due to higher A_{INP}; here, the increase in N_{lim} with decreasing supersaturation is not enough to outweigh the higher INP numbers.

A final point can be made about the strong temperature dependence of the threshold supersaturation for homogeneous nucleation. Within the CNT spectrum, the heterogeneously-formed fraction of N_i actually increases in the SH (Fig. 10) because at the coldest temperatures, the threshold supersaturation for homogeneous nucleation significantly increases, as shown in Figure 1b. A fewer

number of INP are needed to depress the supersaturation enough to inhibit homogeneous nucleation; the dust INP in the CNT simulations are efficient enough to shut down homogeneous nucleation.

3.2 Nucleating aerosol

We consider next which aerosol groups act as INP in the regions of purely heterogeneous nucleation. For PDA08 in Figures 4a and c, both dust and black carbon play a role. Gradients in input temperature and BC contribution both appear around 40°S because the BC threshold supersaturation is a quadratic function of temperature in this spectrum (Figure 1b) [Zuberi et al. 2002]. Below 60°S, the BC contribution is 40% or higher for PDA08. This is unexpected because black carbon sources tend to be continental and anthropogenic, while land coverage and population density are lower in the SH.

For PDA13, dust is by far the primary contributor to $N_{i,het}$ outside of a very localized region of deep convection around the Equator. The correlation for $s_{i,0,DM}$ remains the same between PDA08 and PDA13 and decreases with decreasing temperature because observations show that nucleation on dust generally becomes more efficient at colder temperatures [e.g., Möhler et al. 2006; Field et al. 2006]. PDA13 also uses an updated correlation for $S_{i,0,BC}$, expressed in terms of surface polarity and organic coating:

$$S_{i,0}^{BC} = \tilde{S}_{i,0} + \delta_0^1(F_{OC}, F_{OC,0}, F_{OC,1}) \times [1.2 \times S_i^w(T) - \tilde{S}_{i,0}] \tag{7}$$

where $\tilde{S}_{i,0}$ is a baseline supersaturation of 30%, δ_0^1 is a cubic interpolation over organic coating, F_{OC}, between lower and upper bounds of $F_{OC,0}$ and $F_{OC,1}$ [Köhler et al. 2009; Crawford et al. 2011], and S_i^w is the saturation ratio of vapor with respect to ice at exact water saturation, since minimal nucleation has been observed at water-subsaturated conditions for heavily-coated black carbon [DeMott et al. 1999]. Surface polarity expresses hydrophilicity and is operationally defined as the number of water monolayers adsorbed to the aerosol surface at 50% relative humidity, while the organic coating indicates the fraction of BC surface covered in insoluble organics. These parameters are source-dependent and difficult to determine, but this study assumes a high surface polarity of two monolayers and a low organic coating of 10% to maximize any impact of black carbon (Table 1). Popovicheva et al. 2007 have also shown that these values describe aircraft engine combustion emissions, which would be relevant at this altitude.

The different aerosol contributing to INP concentrations, despite the same framework, can be understood by analyzing the expression for μ_X. Given that the same aerosol size and number distributions have been used in both runs (Table 1), the difference is in the active site density parameterization. The observationally-based terms making up the active site density are a threshold for

water-subsaturated conditions, a threshold for warm sub-zero temperatures, a background aerosol number, and a baseline surface area mixing ratio [Phillips et al. 2008]:

$$n_{S,X} = H_X(S_i,T)\xi(T)\frac{\alpha_X n_{INP,*}}{\Omega_{X,*}} \tag{8}$$

Between PDA08 and PDA13, the portion of aerosol belonging to the BC group, α_{BC}, has increased by 3%, while our input temperatures are too low for the warm sub-zero temperature threshold, $\xi(T)$, to affect N_{INP} calculations. The water-subsaturated threshold, H_X, would completely suppress BC nucleation if F_{OC} were taken to be 100%; experimental evidence has shown that BC nucleation may only occur at water saturation when coating is significant [Möhler et al. 2006]. But we have used F_{OC} of 10% and the threshold supersaturation has actually decreased for PDA13, as shown in Figure 1b. These factors alone actually yield a higher active site density for BC than for dust.

The difference in contributions, then, is the result of changing baseline surface area mixing ratios, $\Omega_{X,*}$. A lower active site density is needed to obtain the same freezing fraction when $\Omega_{X,*}$ is higher. Between PDA08 and PDA13, this parameter decreases fourfold from 2×10^{-6} $\mathrm{m^2\,kg^{-1}}$ to 5×10^{-7} $\mathrm{m^2\,kg^{-1}}$ for dust and increases about threefold from 1×10^{-7} $\mathrm{m^2\,kg^{-1}}$ to 2.7×10^{-7} $\mathrm{m^2\,kg^{-1}}$ for BC. As a result, the freezing fraction of BC is much lower, even if $n_{S,BC}$ is somewhat higher. Dust becomes the primary INP for PDA13 because its freezing fraction has increased. N_i from PDA13 is lower in the NH because the large dust numbers there depress $N_{i,hom}$, as shown in Figures 2 and **??**.

Surface polarity and organic coating parameters are prescribed in these simulations and may be highly variable in the atmosphere. We have chosen a high polarity and low organic coating, so that BC contribution calculations represent an upper bound. For simulations with higher organic coatings, any INP contribution from BC disappears completely. But polarity and coating change with morphology and porosity, which change with source [Popovicheva et al. 2007]. A more detailed consideration of the BC emissions inventory would be needed to more accurately determine these parameters and BC contribution to crystal number. Uncertainty also exists within the BC emissions inventory itself, and this, along with the coating and polarity parameters, will translate to uncertainty in the N_i field.

3.3 Nucleation regime

The sign and magnitude of the insoluble aerosol number sensitivities, $\partial N_i/\partial N_{\mathrm{INP}}$, can be used to elucidate the active nucleation regime. Figure 5 gives an example with the annually-averaged sensitivity of N_i to accumulation mode dust number, $\partial N_i/\partial N_{dust,a}$, for all spectra. In the Southern Hemisphere, sensitivities for PDA08 are of small magnitude ($\mathcal{O}(10^{-4})$) and negative, as homogeneous nucleation dominates. There are localized regions of strong competitive nucleation in sub-Saharan Africa and northern South America, where sensitivities are of larger magnitude ($\mathcal{O}(10^{-3})$)

and negative. Sensitivities throughout most of the Northern Hemisphere are of moderate magnitude and negative, indicating weaker competitive nucleation.

The CNT field exhibits positive sensitivities throughout most of the Northern Hemisphere, delineated in white and indicating purely heterogeneous nucleation. PDA13 also contains regions of purely heterogeneous nucleation but around the Equator in regions of lower updraft and higher INP. When updraft velocity increases significantly - in the region of deep convection over Indonesia or over the Himalayas or Rockies due to orographic lifting - a sufficiently high supersaturation may be generated to exceed the threshold for homogeneous nucleation and induce competitive nucleation. For both the PDA13 and AIDA spectra, regions of large and negative sensitivities, or strong competitive nucleation, appear south of 60°S. INP numbers are considerably lower than N_{lim} here, but the threshold supersaturion for homogeneous nucleation has also increased at these cold temperatures.

The magnitude of negative sensitivities during competitive nucleation reflect the threshold conditions assigned to a given aerosol group. The lower the threshold supersaturation for an aerosol group, the more readily it nucleates and the more effectively it depletes water vapor; this corresponds to larger magnitude $\partial N_i/\partial N_{dust,a}$ before N_{INP} surpasses N_{lim} and purely heterogeneous nucleation begins. PDA13 sensitivities to BC number are of larger magnitude than PDA08 values because $S_{i,0,BC}$ is lower for the polarity and F_{OC} values used here. The cusp of the INP-N_i trace becomes steeper, and the competition for water vapor is stronger in this case.

$\partial N_i/\partial N_{dust,a}$ is of large magnitude ($\mathcal{O}(10^{-2})$) and positive for the AIDA spectrum due to larger predicted INP numbers. These sensitivities decrease in magnitude over the Antarctic because the active site density parameterization has a strong supersaturation dependence at cold temperatures (Supplementary Figure 12). If the temperature decreases by 5 K for a constant supersaturation, the active site density can drop by as much as 25%. The effect of this active site density parameterization on N_i is discussed further in section 3.5. $\partial N_i/\partial N_{dust,a}$ also decreases in magnitude over Indonesia because the large updrafts here generate enough supersaturation that competitive nucleation occurs often and reduces the annually-averaged magnitude of $\partial N_i/\partial N_{\text{INP}}$.

Along with these spatial sensitivity patterns, we look at sensitivity time series without temporal averaging, which show the frequency of occurrence of different nucleation regimes. Infrequent but large magnitude sensitivities can have an important influence on the annual average [Sheyko et al. 2015]. Distributions of both accumulation mode dust number sensitivities and input updraft velocities are presented at (2.9°S, 135°E) over Indonesia and (0.95°N, 64°W) over northern South America in Figure 6. These points are denoted by diamonds in Figure 5. Their annually-averaged sensitivities differ significantly, despite their being in the same latitudinal band with similar aerosol loadings.

The location over Indonesia experiences high updraft more frequently, and the additional supersaturation generation translates to more competitive nucleation and larger magnitude sensitivities in PDA13, almost down to -0.1 LL^{-1}. In PDA08, more supersaturation generation translates to more

frequent homogeneous nucleation and smaller magnitude, less variable sensitivities, on the order of 10^{-3} L L^{-1}. The location over South America has fewer instances of high updraft, so for PDA13, the system cannot always overcome the threshold supersaturation for homogeneous nucleation. Purely heterogeneous nucleation occurs more frequently: Figure 6d has primarily positive sensitivities of small magnitude with an occasional large spike in $\partial N_i/\partial N_{dust,a}$, which always corresponds to a large updraft. Relative to PDA13, PDA08 exhibits stronger water vapor competition: the peaks in Figure 6c are about four times as large as those in Figure 6a. This behavior can be understood in terms of a transition along the INP-N_i trace in Figure 1a: N_i and $\partial N_i/\partial N_{INP}$ respond differently to supersaturation generation based on how many INP the nucleation spectrum predicts.

3.4 INP nucleation efficiency

The positive values of $\partial N_i/\partial N_{INP}$, for which nucleation is purely heterogeneous, can be understood as nucleation efficiencies: those aerosol which act as efficient INP generate a large increase in crystal number for a given increase in aerosol number. Rather than an inherent nucleation efficiency of a certain aerosol group, the sensitivity reflects an INP efficiency given the particular model state. Accumulation mode dust has a mean efficiency of 0.0012% ($\mathcal{O}(10^{-3}\%)$) in PDA08 and 0.079% ($\mathcal{O}(0.1\%)$) in PDA13, while coarse mode dust has a mean efficiency of 0.61% in PDA08 and 0.078% in PDA13. AIDA calculates considerably higher mean efficiency of 1.4% for the accumulation mode and 52% for the coarse mode. Black carbon in PDA08 is 0.03% efficient on average, an order of magnitude higher than the accumulation mode dust. In PDA13, on the other hand, black carbon efficiency is an order lower than accumulation mode dust and skewed toward lower values (not shown). Efficiency of organic aerosol is negligible, on the order of 10^{-5}% and skewed to values as low as 10^{-12}%.

From Equation 3 during purely heterogeneous nucleation,

$$\frac{\partial N_i}{\partial n_X} = 1 - \exp(-n_s(S_i, T)\pi D^2) \tag{9}$$

As the number of embryos per aerosol particle becomes large, the nucleation-active fraction of the aerosol population, which is equivalent to the positive aerosol number sensitivity or the nucleation efficiency, approaches unity. This occurs because the product of active site density and aerosol surface area becomes large enough that an ice embryo should always form on the INP surface. Shifts in the number sensitivities reflect changing contributions to $N_{i,het}$. To illustrate, Figure 7a shows the distribution of a random sample of 5000 daily-averaged dust number sensitivities, when ice nucleation is purely heterogeneous, i.e. $\partial N_i/\partial N_{INP} > 0$. The coarse mode dust number sensitivity is higher, and the accumulation mode dust sensitivity is lower for PDA08 than PDA13 because BC nucleation has been suppressed in the latter. The active site density of PDA08 BC is larger than that of dust under certain conditions (Supplementary Figure 12), meaning that BC efficiencies are

higher than the accumulation mode dust efficiencies because aerosol diameter for the two groups is assumed to be the same. The coarse mode sensitivities or efficiencies are even higher because their surface area is two orders of magnitude larger and outweighs a lower active site density.

The PDA08 distributions also have many more outliers because of the greater competition for water vapor between aerosol groups. The adjoint sensitivities are local in space and time, and in model grid cells without BC, dust in both modes is able to nucleate much more efficiently. In grid cells with more BC, the dust nucleation efficiency is significantly reduced because of the competition for water vapor between the two INP groups. The narrower range of AIDA efficiencies reinforces this point: this spectrum describes nucleation by dust in idealized conditions and no other aerosol compete for water vapor. Its active site parameterization also contains no threshold functions that abruptly reduce nucleation. For application in global models, it may be more effective to use parameterizations from experiments with multiple nucleating aerosol types.

Once an aerosol population has reached its maximum active fraction or efficiency, N_i becomes less sensitive to the number of these aerosol. In PDA13, the coarse mode dust population reaches an upper bound in its efficiency, and N_i sensitivity to coarse mode number decreases to a value comparable to the accumulation mode number. For low active fractions, Equation 9 can be linearized so that $f_{IN} \sim \mathcal{O}(n_s(S_i,T)D^2)$. Given that $n_s \sim \mathcal{O}(10^9\text{m}^{-2})$ and $D \sim \mathcal{O}(10^{-6}\text{m})$ in the coarse mode (Supplementary Figure 12), the maximum active fraction is expected to be on the order of 10^{-3}, which is indeed the value seen in Figure 7.

3.5 Size sensitivity and the active site density

Diameter sensitivities can also be understood in terms of nucleation regime. When nucleation is purely heterogeneous, diameter sensitivity is positive; increasing aerosol diameter increases crystal number because for a given active site density, more surface area increases the number of ice embryos per aerosol. During competitive nucleation, diameter sensitivity becomes negative, as more available surface area for heterogeneous nucleation reduces N_i from $N_{i,hom}$. As with number sensitivity, the magnitude of negative diameter sensitivities reflects how intensely a certain aerosol group can deplete water vapor. The magnitude of positive diameter sensitivities is larger for coarse mode than accumulation mode dust in all spectra (Figure 7); an incremental increase in diameter generates more surface area for larger particles than for smaller particles.

The magnitude of positive diameter sensitivities also reflect active site density. From Equation 3, during purely heterogeneous nucleation,

$$\frac{\partial N_i}{\partial D} = 2\pi D n_X n_s(S_i,T)\exp(-n_s(S_i,T)\pi D^2) \tag{10}$$

which shows that $\partial N_i/\partial D \propto D\text{exp}(-D^2)$ and $\partial N_i/\partial D \propto n_s\text{exp}(-n_s)$. The magnitude of diameter sensitivity first increases, then decreases, with diameter. The larger the diameter, the faster the

sensitivity decreases after its maximum and the larger that maximum sensitivity. Again for active site density, the magnitude of diameter sensitivity first increases then decreases with n_s. And the larger the active site density, the faster the sensitivity decreases after reaching its maximum value. The first effect is stronger because $\partial N_i/\partial D$ is proportional to active site density but to the square of diameter.

Figure 7b is constructed again from a random sample of 5000 daily-averaged dust diameter sensitivities in the purely heterogeneous regime, i.e. $\partial N_i/\partial D_{INP} > 0$. The maximum coarse mode diameter sensitivity is smaller than that of the accumulation mode diameter sensitivity for PDA13 and CNT because the higher number of accumulation mode dust particles outweighs the larger coarse mode surface area. The AIDA and PDA13 spectra tend to reach the same maximum diameter sensitivities (10^{-11} $\mu\mathrm{m cm}^{-3}$ in the coarse mode) as both have reached their maximum active fraction. These features do not characterize the PDA08 distributions because of competition for water vapor with black carbon. Given the higher active site density and equal surface area of black carbon relative to accumulation mode dust, $\partial N_i/\partial D_{dust,a}$ is smaller than in the other spectra. The surface area increase from the addition of a coarse mode dust particle outweighs the higher BC active site density and $\partial N_i/\partial D_{dust,c}$ in PDA08 is comparable to the values in the other spectra. In summary, spectra with large active site densities will be highly sensitive to aerosol diameter over a limited range of these diameters, while spectra with lower active site densities will be less sensitive to aerosol diameter but over a larger range of these diameters. These trends may be convoluted by competition for water vapor with other aerosol species.

3.6 Sensitivity of N_i to temperature and sulfate aerosol

The above discussion has focused on insoluble aerosol sensitivities. Soluble aerosol sensitivities, $\partial N_i/\partial N_{sulf}$, are always positive because the addition of these soluble particles enhance homogeneous nucleation and crystal number, regardless of the insoluble INP profile. When purely heterogeneous nucleation occurs, $\partial N_i/\partial N_{sulf}$ is zero. Sulfate sensitivities are generally on the order of 0.001 $\mathrm{cm}^3\mathrm{cm}^{-3}$ but can be as large as 0.025 $\mathrm{cm}^3\mathrm{cm}^{-3}$ at the coldest temperatures in the SH. This field does not change in magnitude between spectra because the treatment of homogeneous nucleation is identical in all cases. $\partial N_i/\partial N_{sulf}$ is smaller and less influential than the updraft sensitivity fields, similar to the findings of Karcher and Lohmann 2002, for which the aerosol size distribution did not strongly affect the number of nucleated ice crystals.

Temperature sensitivities, $\partial N_i/\partial T$, are generally negative because colder temperatures tend to facilitate ice nucleation. An increase in temperature may exceed the threshold temperature for a certain aerosol group, deactivating it, and allowing homogeneous nucleation to generate a larger N_i. This phenomenon can be observed in both the PDA08 and PDA13 fields, in which positive sensitivities fall exclusively at the outflow of Saharan dust around the equator where input temperature is between 225 and 230 K. These temperatures are in the range at which the water-subsaturated

threshold function for dust drops (T_0^{DM} = -40°C and ΔT = 5°C), so that the primary contributor to heterogeneous nucleation depletes less water vapor and homogeneous nucleation yields higher N_i.

The magnitude of $\partial N_i/\partial T$ is smaller than expected from classical nucleation theory, probably due to counterbalancing effects. For example, as temperature increases so does water vapor diffusivity, which enhances crystal growth and reduces number. But latent heat of sublimation also increases as temperature drops, which slows the crystal growth rate. The homogeneous nucleation coefficient increases by an order of magnitude with only a 30 K drop in temperature [Koop et al. 2000]. The threshold supersaturation for dust, however, also goes down, so that deposition nucleation can more easily inhibit homogeneous nucleation. These various temperature dependencies may cancel out and lead to lower temperature sensitivities within the model. Hoose and Möhler 2012 have noted an intermediate regime in nucleation experiments for which n_s isolines are independent of temperature and change primarily with supersaturation. Similar compensating effects, which cause low temperature sensitivity in the parameterization runs, might also explain this experimentally-observed, temperature-independent regime.

4 Summary

Thorough understanding of nucleated ice crystal variability in global simulations will help improve model representation of cirrus clouds and their radiative forcing. Towards this end, adjoint sensitivity analysis provides a powerful and efficient means of quantifying the prevalent ice nucleation regime, active site density and inputs driving temporal and spatial variability in the model output. From analysis of a single GCM simulation for each nucleation spectrum, using CAM 5.1 and current day emissions, we have shown the following results:

- *Nucleation regime is determined by INP, but N_i is determined by threshold conditions and INP abundance.* During a simulation, the number of ice-nucleating particles predicted by a nucleation spectrum determines its nucleation regime, or equivalently where the system "sits" along the INP-N_i trace. Threshold supersaturation and the number of INP relative to the limiting number determine the nucleated ice crystal number. Lower ice crystal numbers can be calcualted in spite of higher INP, if certain aerosol have less stringent threshold supersaturations, because $s_{i,0,X}$ affects the steepness and depth of the competitive cusp on the INP-N_i trace. At the coldest temperatures, strong supersaturation dependence of active site parameterizations may also reduce N_i. In addition, the number of INP only dictates ice crystal number relative to the limiting number to prevent homogeneous nucleation in this framework. If N_{lim} calculated in one spectrum is lower relative to another, this spectrum may still calculate higher crystal number with fewer ice-nucleating particles.

- *The baseline surface area mixing ratio, $\Omega_{X,*}$, strongly affects which INP contribute to N_i. The suppression of certain INP groups manifests as shifts in the aerosol number sensitivity distri-*

butions. Dust contribution to heterogeneously-formed number dominates on a global scale for PDA13 runs. Deconstructing the active site density parameterization shows that this suppression is due to a fourfold decrease in $\Omega_{DM,*}$ and threefold increase in $\Omega_{BC,*}$, which increases the freezing fraction of dust significantly. Although the surface polarity and organic coating parameters remain unconstrained, we have chosen values which would maximize the black carbon ice-nucleating activity. The model predicts that black carbon contribution is negligible to N_i at this pressure level, if the PDA13 treatment is not too conservative.

Differing aerosol contributions to N_i manifest in the number sensitivity distributions. When black carbon does not act as an INP and there is no competition for water vapor between aerosol types, the sensitivity to accumulation mode dust number increases and the sensitivity to coarse mode dust number decreases. Glassy aerosol has a small, but regionally important and seasonally-dependent contribution in PDA13.

– *The sign of ice crystal number sensitivity to insoluble aerosol number or diameter indicates nucleation regime.* When insoluble aerosol number or diameter sensitivities are small and negative, nucleation is predominantly homogeneous. When these values become large and negative, competitive nucleation has initiated, and when the values become positive, nucleation is purely heterogeneous. The spatial distributions of insoluble aerosol number sensitivity, as in Figure 5, can help explain those of crystal number in Figure 2. Temporal distributions of sensitivity can also be used to understand regime shifts along the INP-N_i trace. Spectra that predict different INP numbers may respond differently to additional supersaturation generation.

– *The magnitude of positive aerosol number sensitivity reflects heterogeneous nucleation efficiency. The sensitivity of positive diameter sensitivity reflects active site density.* When nucleation is purely heterogeneous, the magnitude of aerosol number sensitivity can be understood as a nucleation efficiency. The range of efficiencies is limited when there is no competition for water vapor between aerosol groups. Crystal number is more sensitive to the aerosol species with higher associated surface areas, until those species reach their maximum active fractions. In the same vein, crystal number is more sensitive to the size of larger aerosol, until the maximum active fraction is obtained. An incremental increase in the diameter of a large particle yield greater surface area but exhausts the active site density more quickly.

– *Temperature sensitivities are of smaller magnitude than expected with classical nucleation theory because of compensating temperature dependencies.* Limited sensitivities to temperature reflect the empirically observed “intermediate temperature regime," where supersaturation is more influential on nucleation.

Appendix A

BN09 - Barahona and Nenes 2009 cirrus formation parameterization

$N_{i,het}$ - Heterogeneously-formed ice crystal number

INP - Ice-nucleating particles

s_i - Supersaturation of water vapor with respect to ice

PDA08 - Phillips, DeMott, and Andromache 2008 INP spectrum

PDA13 - Phillips et al. INP spectrum, updated from 2008

AIDA - Heterogeneous INP spectra derived from Aerosol Interaction and Dynamics in the Atmosphere cloud chamber data

$N_{i,het}$ - Number of heterogeneously-nucleated ice crystals

$N_{i,hom}$ - Number of homogeneously-nucleated ice crystals

N_{lim} - Limiting number of INP to prevent homogeneous nucleation

s_{max} - Maximum supersaturation which develops within the cloud parcel

s_{hom} - Threshold supersaturation for homogeneous nucleation

S_i - Saturation ratio of water vapor with respect to ice

μ_X - Number of ice embryos per aerosol surface

$\partial N_i/\partial D_{dust,c}$ - Nucleated ice crystal number sensitivity to coarse mode dust diameter

$\partial N_i/\partial D_{dust,a}$ - Nucleated ice crystal number sensitivity to accumulation mode dust diameter

$\partial N_i/\partial N_{dust,c}$ - Nucleated ice crystal number sensitivity to coarse mode dust number

$\partial N_i/\partial N_{dust,a}$ - Nucleated ice crystal number sensitivity to accumulation mode dust number

Acknowledgements. This work was made possible through support from DOE EaSM. SS gratefully acknowledges support from a National Aeronautics and Space Administration Earth and Space Science Fellowship. We would like to thank two anonymous reviewers for their thorough and insightful feedback, in particular for suggestions about measurement-model comparison. Data in Figure 3 comes from Andrew Heymsfield's VIPS and Paul Lawson's TDS measurements aboard the WB57 during MACPEX and from Paul Lawson's F-FSSP measurements aboard the SPEC Learjet during SPARTICUS. Thanks also to Heike Kalesse for the use of processed vertical motion data from SPARTICUS.

References

Barahona, D.: On the ice nucleation spectrum, Atmos. Chem. Phys., 12, 3733–3752, doi:10.5194/acp-12-3733-2012, 2012.

Barahona, D. and Nenes, A.: Parameterization of cirrus cloud formation in large-scale models: Homogeneous nucleation, J. Geoph. Res., 113, doi:10.1029/2007JD009355, 2008.

Barahona, D. and Nenes, A.: Parameterizing the competition between homogeneous and heterogeneous freezing in cirrus cloud formation - monodisperse ice nuclei, Atmos. Chem. Phys., 9, 369–381, doi:10.5194/acp-9-369-2009, 2009a.

Barahona, D. and Nenes, A.: Parameterizing the competition between homogeneous and heterogeneous freezing in ice cloud formation - polydisperse ice nuclei, Atmos. Chem. Phys., 9, 5933–5948, doi:10.5194/acp-9-5933-2009, 2009b.

Barahona, D. and Nenes, A.: Dynamical states of low temperature cirrus, Atmos. Chem. Phys., 11, 3757–3771, doi:10.5194/acp-11-3757-2011, 2011.

Barahona, D., Rodriguez, J., and Nenes, A.: Sensitivity of the global distribution of cirrus ice crystal concentration to heterogeneous freezing, J. Geoph. Res., 115, doi:10.1029/2010JD014273, 2010.

Barahona, D., Molod, A., Bacmeister, J., Nenes, A., Gettleman, A., Morrison, H., Phillips, V., and Eichmann, A.: Development of two-moment cloud microphysics for liquid and ice within the NASA Goddard Earth Observing System model (GEOS-5), Geosci. Model Devel., 7, 1733–1766, doi:10.5194/gmd-7-1733-2014, 2014.

Betancourt, R. M. and Nenes, A.: Characteristic updrafts for computing distribution-averaged cloud droplet number and stratocumulus cloud properties, J. Geoph. Res., 115, doi:10.1029/2009JD013233, 2010.

Boucher, O., Randall, D., Artaxo, P., Bretherton, C., Feingold, G., Forster, P., Kerminen, V.-M., Kondo, Y., Liao, H., Lohmann, U., Rasch, P., Sathessh, S., Sherwood, S., Stevens, B., and Zhang, X.: Clouds and Aerosols. In: *Climate Change 2013: The Physical Science Basis. Contribution of Working Group I to the Fifth Assessment Report of the Intergovernmental Panel on Climate Change*, Cambridge University Press, 2013.

Brewer, J.: Evidence for a world circulation provided by the measurements of helium and water vapour distribution in the stratosphere, Q. J. Roy. Meteor. Soc., 75, 351–363, doi:10.1002/qj.49707532603, 1949.

Broadley, S., Murray, B., Herbert, R., Atkinson, J., Dobbie, S., Malkin, T., Condliffe, E., and Neve, L.: Immersion mode heterogeneous ice nucleation by an illite rich powder representative of atmospheric mineral dust, Atmos. Chem. Phys., 12, 287–307, doi:10.5194/acp-12-287-2012, 2012.

Capps, S., Henze, D., Hakami, A., Russell, A., and Nenes, A.: ANISORROPIA: the adjoint of the aerosol thermodynamic model ISORROPIA, Atmos. Chem. Phys., 12, 527–543, doi:10.5194/acp-12-527-2012, 2012.

Chen, J.-P., Hazra, A., and Levin, Z.: Parameterizing ice nucleation rates using contact angle and activation energy derived from laboratory data, Atmos. Chem. Phys., 8, 7431–7449, doi:10.5194/acp-8-7431-2008, 2008.

Chen, T., Rossow, W. B., and Zhang, Y.: Radiative effects of cloud-type variations, J. Clim., 13, 264–286, doi:10.1175/1520-0442(2000)013<0264:REOCTV>2.0.CO;2, 2000.

Connolly, P. J., Möhler, O., Field, P. R., Saathoff, H., Burgess, R., Choularton, T., and Gallagher, M.: Studies of heterogeneous freezing by three different desert dust samples, Atmos. Chem. Phys., 9, 2805–2824, doi:10.5194/acp-9-2805-2009, 2009.

Cox, S. J., Kathmann, S. M., Slater, B., and Michaelides, A.: Molecular simulations of heterogeneous ice nucleation. I. Controlling ice nucleation through surface hydrophilicity, J. Chem. Phys., 142, doi:10.1063/1.4919714, 2015.

Crawford, I., Möhler, O., Schnaiter, M., Saathoff, H., Liu, D., McMeeking, G., Linke, C., Flynn, M., Bower, K. N., Connolly, P. J., Gallagher, M. W., and Coe, H.: Studies of propane flame soot acting as heterogeneous ice nuclei in conjunction with single particle soot photometer measurements, Atmos. Chem. Phys., 11, 9549–9561, doi:10.5194/acp-11-9549-2011, 2011.

Curry, J. A. and Khvorostyanov, V. I.: Assessment of some parameterizations of heterogeneous ice nucleation in cloud and climate models, Atmos. Chem. Phys., 12, 1151–1172, doi:10.5194/acp-12-1151-2012, 2012.

Cziczo, D., Froyd, K., Hoose, C., Jensen, E., Diao, M., Zondlo, M., Smith, J., Twohy, C., and Murphy, D.: Clarifying the dominant sources and mechanisms of cirrus cloud formation, Science, 340, 1320–1324, doi:10.1126/science.1234145, 2013.

d'Almeida, G.: On the variability of desert aerosol radiative characteristics, J. Geophys. Res., 92, 3017–3026, doi:10.1029/JD092iD03p03017, 1987.

DeMott, P., Chen, Y., Kreidenweis, S., Rogers, D., and Sherman, D.: Ice formation by black carbon particles, Geophys. Res. Letters, 26, 2429–2432, doi:10.1029/1999GL900580, 1999.

DeMott, P. J., Prenni, A. J., Liu, X., Kreidenweis, S. M., Petters, M. D., Twohy, C. H., Richardson, M. S., Eidhammer, T., and Rogers, D. C.: Predicting global atmospheric ice nuclei distributions and their impacts on climate, Proc. Nat. Acad. Sci., doi:10.1073/pnas.0910818107, 2010.

Dentener, F., Kinne, S., Bond, T., Boucher, O., Cofala, J., Generoso, S., Ginoux, P., Gong, S., Hoelzemann, J. J., Ito, A., Marelli, L., Penner, J. E., Putaud, J.-P., Textor, C., Schulz, M., van der Werf, G. R., and Wilson, J.: Emissions of primary aerosol and precursor gases in the years 2000 and 1750 prescribed data-sets for AeroCom, Atmos. Chem. Phys., 6, 4321–4344, doi:10.5194/acp-6-4321-2006, 2006.

Errico, R. M.: What is an adjoint model?, Bull. Amer. Meteo. Soc., pp. 2577–2591, doi:10.1175/1520-0477(1997), 1997.

Field, P., Möhler, O., Connolly, P., Krämer, M., Cotton, R., Heymsfield, A., Saathoff, H., and Schnaiter, M.: Some ice nucleation characteristics of Asian and Saharan desert dust, Atmos. Chem. Phys., 6, 2991–3006, doi:10.5194/acp-6-2991-2006, 2006.

Giering, R. and Kaminski, T.: Recipes for Adjoint Code Construction, ACM Trans. Mathematical Software, 24, 437–474, doi:10.1145/293686.293695, 1998.

Guo, H., Liu, Y., Daum, P., Senum, G., and Tao, W.-K.: Characteristics of vertical velocity in marine stratocumulus: comparison of large eddy simulations with observations, Env. Res. Letters, 3, doi:10.1088/1748-9326/3/4/045020, 2008.

Hakami, A., Henze, D., Seinfeld, J., Singh, K., Sandu, A., Kim, S., Byun, D., and Li, Q.: The Adjoint of CMAQ, Env. Sci. Tech., 41, 7807–7817, doi:10.1021/es070944p, 2007.

Hascoët, L. and Pascual, V.: TAPENADE 2.1 user's guide, INRIA Technical Report RT-0300, p. 78, 2004.

Hiranuma, N., Hoffmann, N., Kiselev, A., Dreyer, A., Zhang, K., Kulkarni, G., Koop, T., and Möhler, O.: Influence of surface morphology on the immersion mode ice nucleation efficiency of hematite particles, Atmos. Chem. Phys., 14, 2315–2324, doi:10.5194/acp-14-2315-2014, 2014.

Hoose, C. and Möhler, O.: Heterogeneous ice nucleation on atmospheric aerosols: a review of results from laboratory experiments, Atmos. Chem. Phys., 12, 12 531–12 621, doi:10.5194/acpd-12-12531-2012, 2012.

Jensen, E. J., Kinne, S., and Toon, O. B.: Tropical cirrus cloud radiative forcing - sensitivity studies, Geophys. Res. Lett., 21, 2023–2026, doi:10.1029/94GL01358, 1994.

Jensen, E. J., Pfister, L., Bui, T. P., Lawson, P., and Baumgardner, D.: Ice nucleation and cloud microphysical properties in tropical tropopause layer cirrus, Atmos. Chem. Phys., 10, 1369–1384, doi:10.5194/acp-10-1369-2010, 2010.

Jensen, E. J., Lawson, R. P., Bergman, J. W., Pfister, L., Bui, T. P., and Schmitt, C. G.: Physical processes controlling ice concentrations in synoptically forced, midlatitude cirrus, J. Geophys. Res., 118, 5348–5360, doi:10.1002/jgrd.50421, 2013.

Kalesse, H. and Kollias, P.: Climatology of high cloud dynamics using profiling ARM Doppler Radar observations, J. Clim., 26, 6340–6359, doi:10.1175/JCLI-D-12-00695.1, 2013.

Karcher, B. and Lohmann, U.: A Parameterization of cirrus cloud formation: Homogeneous freezing including effects of aerosol size, J. Geophys. Res., 107, doi:10.1029/2001JD001429, 2002.

Karydis, V., Capps, S., Russell, A., and Nenes, A.: Adjoint sensitivity of global cloud droplet number to aerosol and dynamical parameters, Atmos. Chem. Phys., 12, 9041–9055, doi:10.5194/acp-12-9041-2012, 2012.

Köhler, K. A., DeMott, P. J., Kreidenweis, S. M., Popovicheva, O. B., Petters, M. D., Carrico, C. M., Kireeva, E. D., Khokhlova, T. D., and Shonija, N. K.: Cloud condensation nuclei and ice nucleation activity of hydrophobic and hydrophilic soot particles, Phys. Chem. Chem. Phys., 11, 7906–7920, doi:10.1039/B905334B, 2009.

Koop, T., Luo, B., Tsias, A., and Peter, T.: Water activity as the determinant for homogeneous ice nucleation in aqueous solutions, Nature, 406, 611–614, doi:10.1038/35020537, 2000.

Krämer, M., Schiller, C., Afchine, A., Bauer, R., Gensch, I., Mangold, A., Schlicht, S., Spelten, N., Sitnikov, N., Borrmann, S., de Reus, M., and Spichtinger, P.: Ice supersaturations and cirrus cloud crystal numbers, Atmos. Chem. Phys., 9, 3505–3522, doi:10.5194/acp-9-3505-2009, 2009.

Kulkarni, G., Fan, J., Comstock, J., Liu, X., and Ovchinnikov, M.: Laboratory measurements and model sensitivity studies of dust deposition ice nucleation, Atmos. Chem. Phys., 12, 7295–7308, doi:10.5194/acp-12-7295-2012, 2012.

Lamarque, J.-F., Bond, T. C., Eyring, V., Granier, C., Heil, A., Klimont, Z., Lee, D., Liousse, C., Mieville, A., Owen, B., Schultz, M. G., Shindell, D., Smith, S. J., Stehfest, E., Van Aardenne, J., Cooper, O. R., Kainuma, M., Mahowald, N., McConnell, J. R., Naik, V., Riahi, K., and van Vuuren, D. P.: Historical (1850 - 2000) gridded anthropogenic and biomass burning emissions of reactive gases and aerosols: methodology and application, Atmos. Chem. Phys., 10, 7017–7039, doi:10.5194/acp-10-7017-2010, 2010.

Lin, R.-F., Starr, D. O., Reichardt, J., and DeMott, P. J.: Nucleation in synoptically forced cirrostratus, J. Geophys. Res., 110, doi:10.1029/2004JD005362, 2005.

Liu, X. and Penner, J.: Ice nucleation parameterization for global models, Met. Zeit., 14, 499–514, doi:10.1127/0941-2948/2005/0059, 2005.

Liu, X., Easter, R. C., Ghan, S. J., Zaveri, R., Rasch, P., Shi, X., Lamarque, J.-F., Gettelman, A., Morrison, H., Vitt, F., Conley, A., Park, S., Neale, R., Hannay, C., Ekman, A. M. L., Hess, P., Mahowald, N., Collins, W., Iacono, M. J., Bretherton, C. S., Flanner, M. G., and Mitchell, D.: Toward a minimal representation of

aerosols in climate models: description and evaluation in the Community Atmosphere Model CAM5, Geo. Model Develop., 5, 709–739, doi:10.5194/gmd-5-709-2012, 2012a.

Liu, X., Shi, X., Zhang, K., Jensen, E. J., Gettelman, A., Barahona, D., Nenes, A., and Lawson, P.: Sensitivity studies of dust ice nuclei effect on cirrus clouds with the Community Atmosphere Model CAM5, Atmos. Chem. Phys., 12, 12 061–12 079, doi:10.5194/acp-12-12061-2012, 2012b.

Lupi, L., Hudait, A., and Molinero, V.: Heterogeneous Nucleation of Ice on Carbon Surfaces, Journal of the American Chemical Society, 136, 3156–3164, doi:10.1021/ja411507a, 2014.

Marcolli, C., Gedamke, S., Peter, T., and Zobrist, B.: Efficiency of immersion mode ice nucelation on surrogates of mineral dust, Atmos. Chem. Phys., 7, 5081–5091, doi:10.1007/978-1-4020-6475-3, 2007.

Meyers, M., DeMott, P., and Cotton, R.: New primary ice-nucleation parameterization in an explicit cloud model, J. Appl. Meteorol., 31, 708–721, doi:10.1175/1520-0450(1992)031, 1992.

Möhler, O., Field, P. R., Connolly, P., Benz, S., Saathoff, H., Schnaiter, M., Wagner, R., Cotton, R., Krämer, M., Mangold, A., and Heymsfield, A. J.: Efficiency of the deposition mode ice nucleation on mineral dust particles, Atmos. Chem. Phys., 6, 3007–3021, doi:10.5194/acp-6-3007-2006, 2006.

Morales-Betancourt, R. and Nenes, A.: Understanding the contributions of aerosol properties and parameterization discrepancies to droplet number variability in a global climate model, Atmos. Chem. Phys., 14, 4809–4826, doi:10.5194/acp-14-4809-2014, 2014.

Morales-Betancourt, R., Lee, D., Oreopoulos, L., Sud, Y. C., Barahona, D., and Nenes, A.: Sensitivity of cirrus and mixed-phase clouds to the ice nuclei spectra in McRAS-AC: single column model simulations, Atmos. Chem. Phys., 12, 10 679–10 692, doi:10.5194/acp-12-10679-2012, 2012.

Murary, B., O'Sullivan, D., Atkinson, J., and Webb, M.: Ice nucleation by particles immersed in supercooled cloud droplets, Chem. Soc. Rev., 41, 6519–6554, doi:10.1039/c2cs35200a, 2012.

Niedermeier, D., Hartmann, S., Shaw, R. A., Covert, D., Mentel, T. F., Schneider, J., Poulain, L., Reitz, P., Spindler, C., Clauss, T., Kiselev, A., Hallbauer, E., Wex, H., Mildenberger, K., and Stratmann, F.: Heterogeneous freezing of droplets with immersed mineral dust particles – measurements and parameterization, Atmos. Chem. Phys., 10, 3601–3614, doi:10.5194/acp-10-3601-2010, 2010.

Niemand, M., Möhler, O., Vogel, B., Vogel, H., and Hoose, C.: A particle-surface-area-based parameterization of immersion freezing on desert dust particles, J. Atmos. Sci., 69, 3077–3092, doi:10.1175/JAS-D-11-0249.1, 2012.

Phillips, V., DeMott, P., and Andronache, C.: An empirical parameterization of heterogeneous ice nucleation for multiple chemical species of aerosol, J. Atmos. Sci., 65, 2757–2783, doi:10.1175/2007JAS2546.1, 2008.

Phillips, V., DeMott, P., Andronache, C., Pratt, K., Prather, K., Subramanian, R., and Twohy, C.: Improvements to an empirical parameterization of heterogeneous ice nucleation and its comparison with observations, J. Atmos. Sci., 70, 378–409, doi:10.1175/JAS-D-12-080.1, 2013.

Popovicheva, O., Persiantseva, N., Shonija, N., DeMott, P., Koehler, K., Petters, M., Kreidenweis, S., Tishkova, V., Demirdjian, B., and Suzanne, J.: Water interaction with hydrophobic and hydrophilic soot particles, Phys. Chem. Chem. Phys., 10, 2332–2344, doi:10.1039/b718944n, 2007.

Prenni, A., Harrington, J., Tjernström, M., DeMott, P., Avramov, A., Long, C., Kreidenweis, S., Olsson, P., and Verlinde, J.: Can Ice-Nucleating Aerosols Affect Arctic Seasonal Climate?, Bull. Amer. Meteo. Soc., 88, 541–550, doi:10.1175/BAMS-88-4-541, 2007.

Pruppacher, H. and Klett, J.: Microphysics of clouds and precipitation, 2nd edition, Kluwer Academic Publishers, Boston, MA, 1997.

Reinhardt, A. and Doye, J. P. K.: Effects of surface interactions on heterogeneous ice nucleation for a monatomic water model, J. Chem. Phys., 141, doi:10.1063/1.4892804, 2014.

Ren, C. and MacKenzie, A.: Cirrus parameterization and the role of ice nuclei, Q.J.R. Meteorol. Soc., 131, 1585–1605, doi:10.1256/qj.04.126, 2005.

Savre, J., Ekman, A., Svensson, G., and Tjernström, M.: Parameterizing ice nucleation ability of mineral dust particles in the deposition mode: numerical investigations using large eddy simulation, AIP Proceedings, 922, doi:10.1063/1.4803422, 2013.

Sheyko, B., Sullivan, S. C., Morales-Betancourt, R., Capps, S., Barahona, D., Shi, X., Liu, X., and Nenes, A.: Quantifying sensitivities of ice crystal number and sources of ice crystal number variability in CAM 5.1 using the adjoint of a physically based cirrus formation parameterization, J. Geophys. Res., 120, doi:10.1002/2014JD022457, 2015.

Shi, X.-J., Liu, X., and Zhang, K.: Effects of preexisting ice crystals on cirrus clouds and comparison between different ice nucleation parameterizations with the Community Atmosphere Model (CAM5), Atmos. Chem. Phys., 15, 1503–1520, doi:10.5194/acp-15-1503-2015, 2015.

Skrotzki, J., Connolly, P., Schnaiter, M., Saathoff, H., Möhler, O., Wagner, R., Niemand, M., Ebert, V., and Leisner, T.: The accommodation coefficient of water molecules on ice: cirrus cloud studies at the AIDA simulation chamber, Atmos. Chem. Phys., 13, 4451–4466, doi:10.5194/acp-13-4451-2013, 2013.

Spichtinger, P. and Gierens, K. M.: Modelling of cirrus clouds - Part 1b: Structuring cirrus clouds by dynamics, Atmos. Chem. Phys., 9, 707–719, doi:10.5194/acp-9-707-2009, 2009.

Spichtinger, P. and Krämer, M.: Tropical tropopause ice clouds: a dynamic approach to the mystery of low crystal numbers, Atmos. Chem. Phys., 13, 9801–9818, doi:10.5194/acp-13-9801-2013, 2013.

Steinke, I., Hoose, C., Möhler, O., Connolly, P., and Leisner, T.: A new temperature and humidity dependent surface site density approach for deposition ice nucleation, Atmos. Chem. Phys., 14, 18 499–18 539, 2014.

Vali, G.: Interpretation of freezing nucleation experiments: singular and stochastic; sites and surfaces, Atmos. Chem. Phys., 14, 1711–1750, doi:10.5194/acp-14-5271-2014, 2014.

Wang, Y., Liu, X., Hoose, C., and Wang, B.: Different contact angle distributions for heterogeneous ice nucleation in the Community Atmosphere Model version 5, Atmos. Chem. Phys., 14, 10 411–10 430, doi:10.5194/acp-14-10411-2014, 2014.

Whitby, K.: The physical characteristics of sulfur aerosols, Atm. Env., 41, 25–49, doi:10.1016/0004-6981(78)90196-8, 2007.

Xie, S., Liu, X., Zhao, C., and Zhang, Y.: Sensitivity of CAM5-simulated Arctic clouds and radiation to nucleation parameterization, J. Clim., 26, 5981–5999, doi:10.1175/JCLI-D-12-00517.1, 2013.

Zhang, K., Liu, X., Wang, M., Comstock, J. M., Mitchell, D., Mishra, S., and Mace, G. G.: Evaluating and constraining ice cloud parameterizations in CAM5 using aircraft measurements from thte SPARTICUS campaign, Atmos. Chem. Phys., 13, 4963–4982, doi:10.5194/acp-13-4963-2013, 2013.

Zuberi, B., Bertram, A., Cassa, C., Molina, L., and Molina, M.: Heterogeneous nucleation of ice in ammonium sulfate-water particles with mineral dust immersions, Geophys. Res. Letters, 29, doi:10.1029/2001GL014289, 2002.

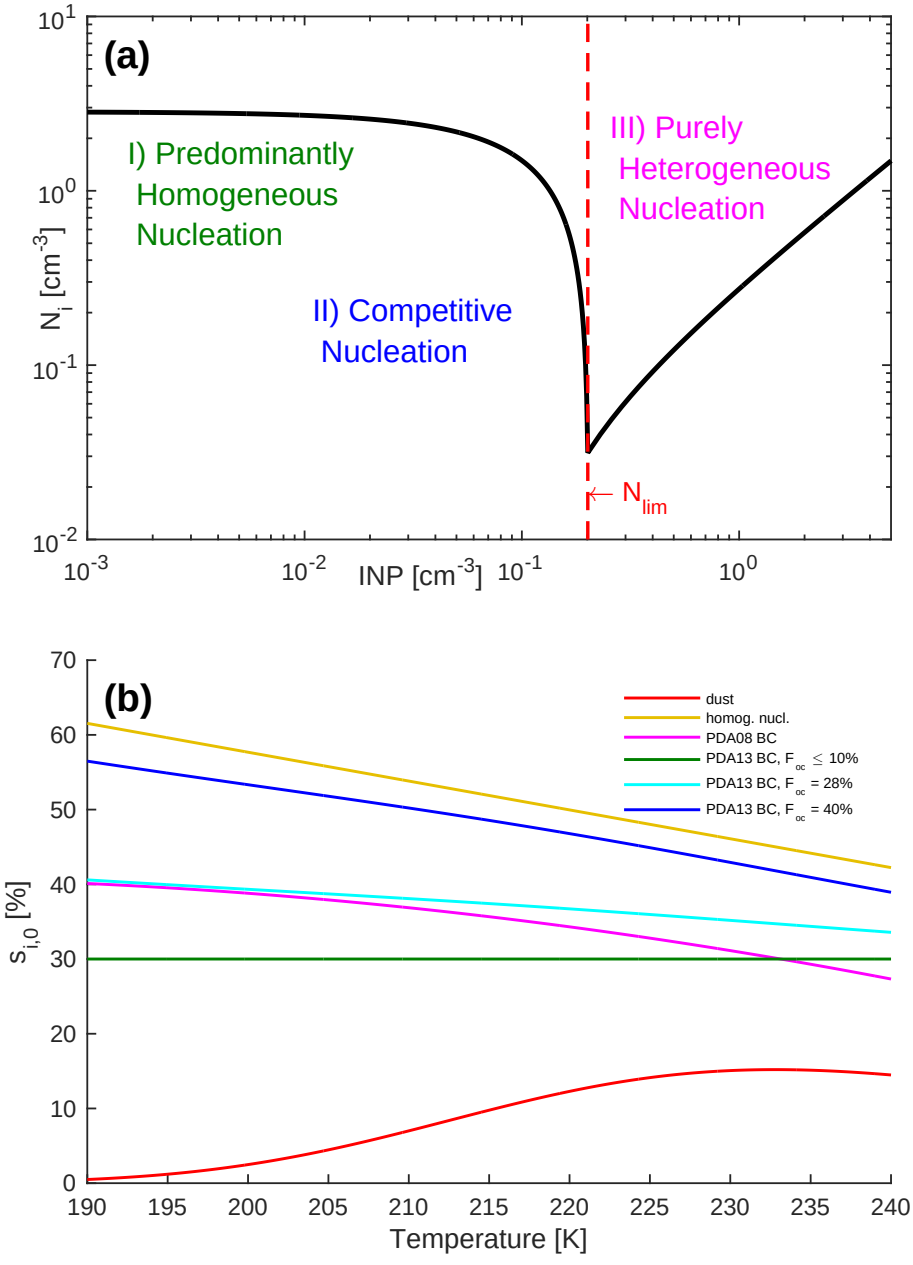

Figure 1. **(a)** Nucleation regimes of cirrus in the log-log INP-ice crystal number space. At low INP numbers, nucleation is predominantly homogeneous. At intermediate INP numbers, nucleation is competitive between homogeneous and heterogeneous. Beyond the threshold INP number, N_{lim}, nucleation is purely heterogeneous; **(b)** threshold supersaturations for homogeneous nucleation and heterogeneous nucleation on mineral dust and BC with different organic coatings, F_{OC} between 190 and 240 K for the PDA08 and PDA13 nucleation spectra. Both use the same correlation for dust.

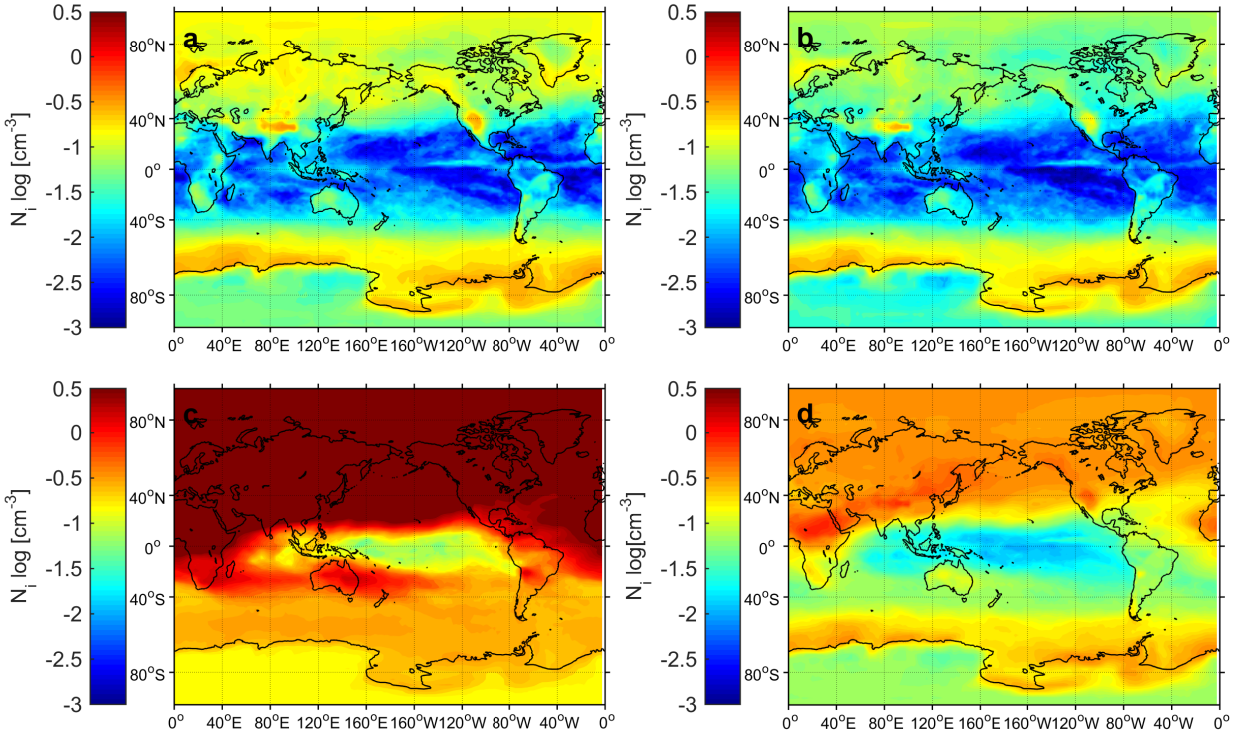

Figure 2. Annually-averaged output nucleated ice crystal number, N_i from the cirrus formation parameterization for **(a)** PDA08, **(b)** PDA13, **(c)** CNT, **(d)** AIDA nucleation spectra.

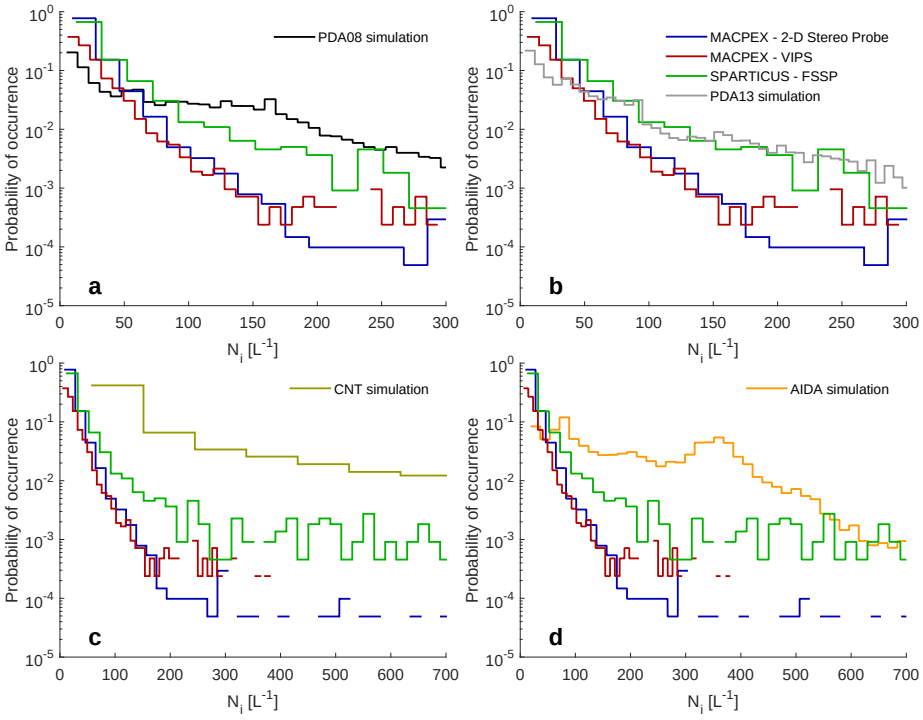

Figure 3. Measurement-model comparison of probability distributions in ice crystal number concentrations. Data distributions come from the Video Ice Particle Sampler (VIPS) and the Two-Dimensional Stereo (2DS) Probe during April 2011 of the MACPEX campaign and the Foward-Scattering Spectrometer (FSSP) during January 2010 of the SPARTICUS campaigns. Only measurements from the 10-20 μm bin of the VIPS; the 5-15 μm bin of the 2DS; and the 0.89, 1.90, 3.80, 5.85, 8.30, 11.45, 14.25, 17.15, and 20.45 μm-centered bins of the 2DS are used, as approximations to the newly-nucleated ice crystal number. Measurements are also filtered for altitudes of 232 $\pm$ 20 hPa and for uniformity, lasting at least 45 s. Distributions of simulation output, i.e. of the annually-averaged output nucleated ice crystal number, N_i, as in Figure 2, are shown using the **(a)** PDA08, **(b)** PDA13, **(c)** CNT, and **(d)** AIDA nucleation spectra. Different independent axes are used in panels **(c)** and **(d)**.

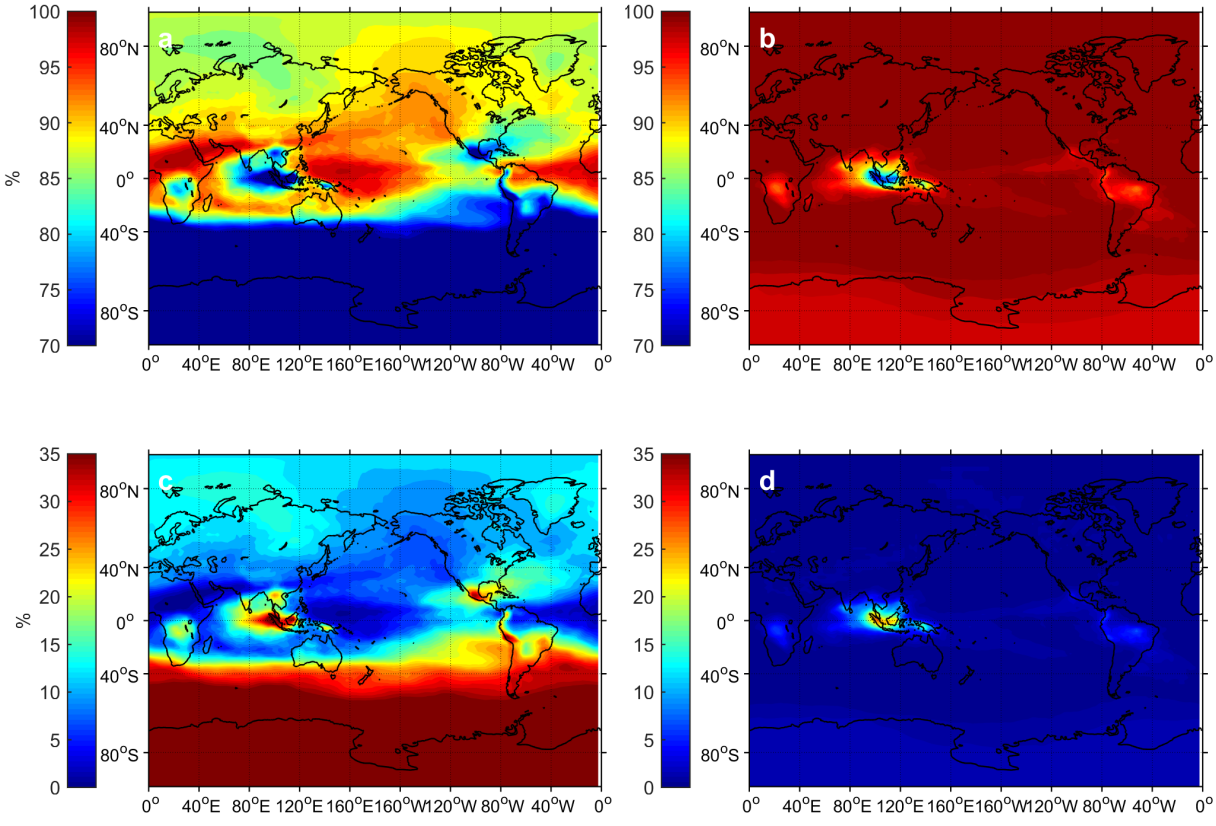

Figure 4. Annually-averaged contributions of dust and BC to heterogeneously-formed ice crystal number. **(a)** Dust contribution in PDA08; **(b)** dust contribution in PDA13; **(c)** black carbon contribution in PDA08; and **(d)** black carbon contribution in PDA13.

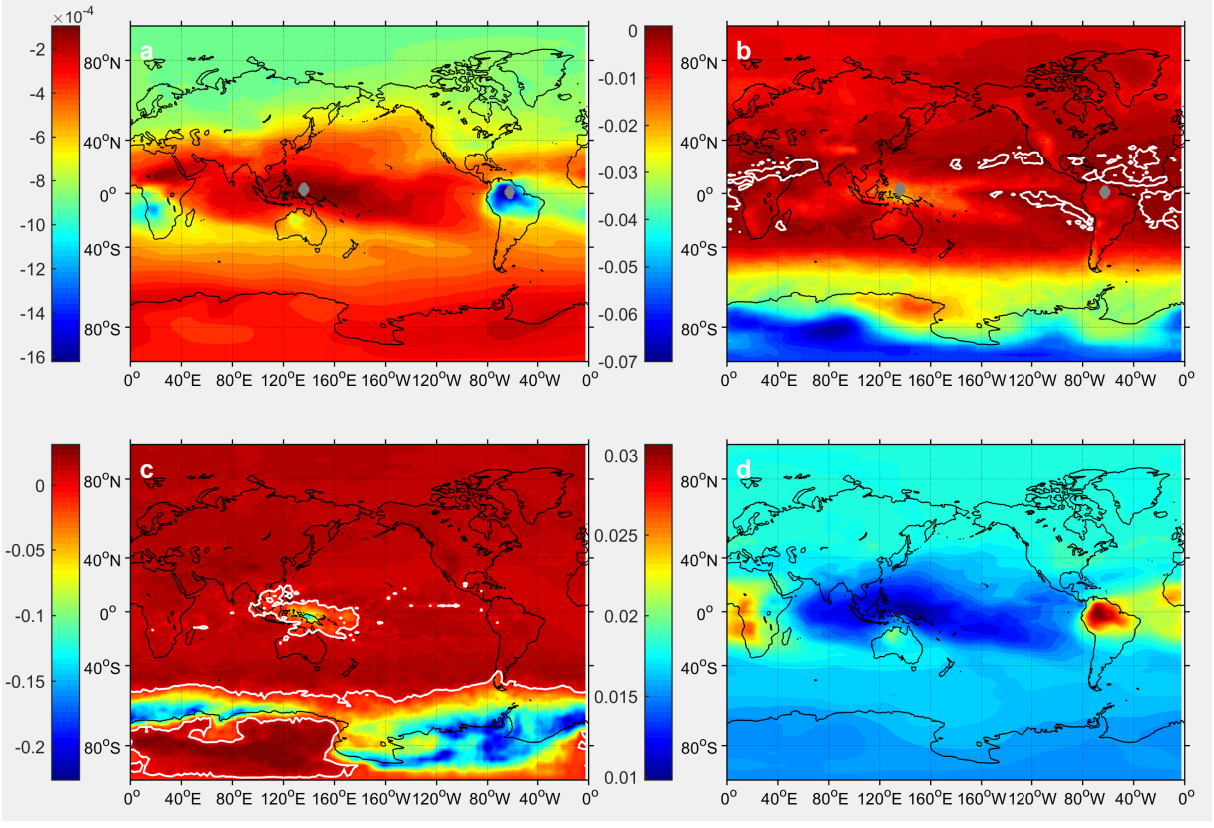

Figure 5. Annually-averaged accumulation mode dust number sensitivities for **(a)** PDA08, **(b)** PDA13, **(c)** CNT, and **(d)** AIDA.

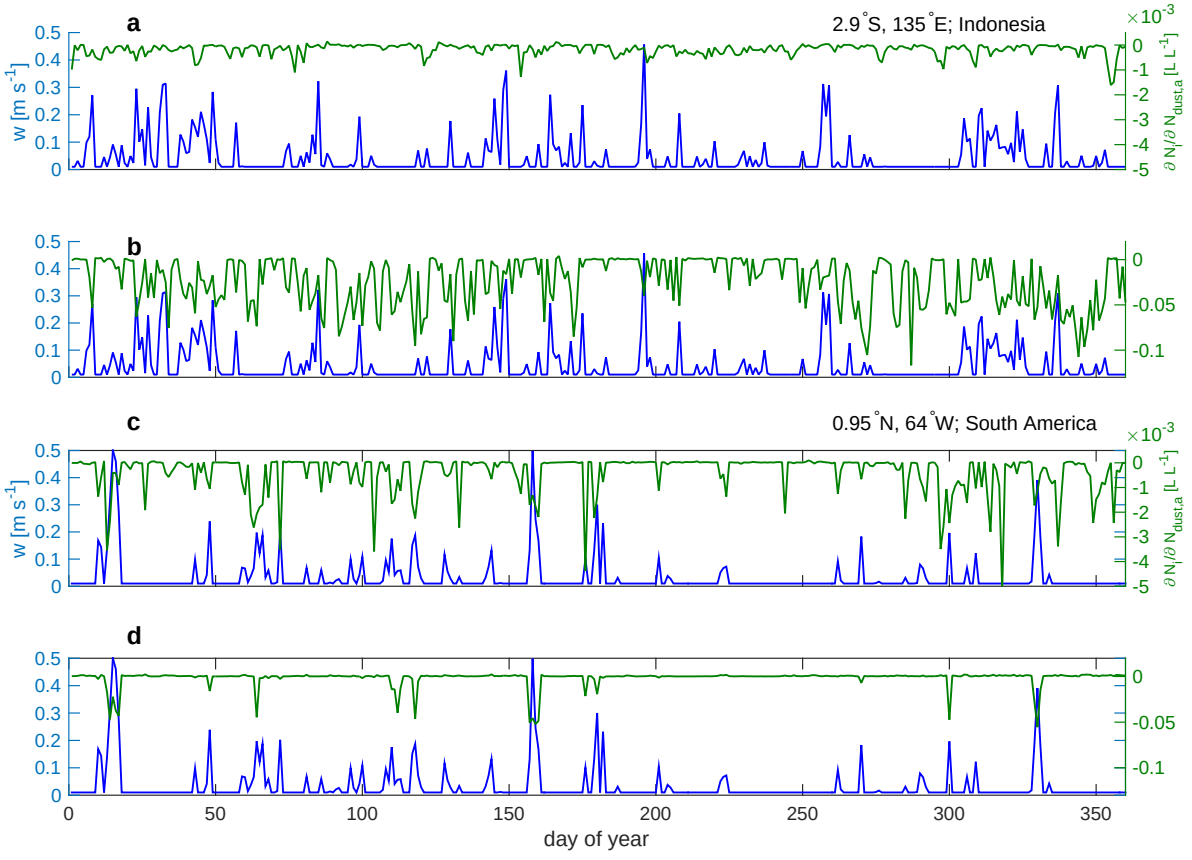

Figure 6. Time series of accumulation mode dust number sensitivities (green, in LL^{-1}) and input updraft velocities (blue, in ms^{-1}) over Indonesia at 2.9°S, 135°E for **(a)** PDA08 and **(b)** PDA13; and over South America at 0.95°N , 64°W for **(c)** PDA08 and **(d)** PDA13.

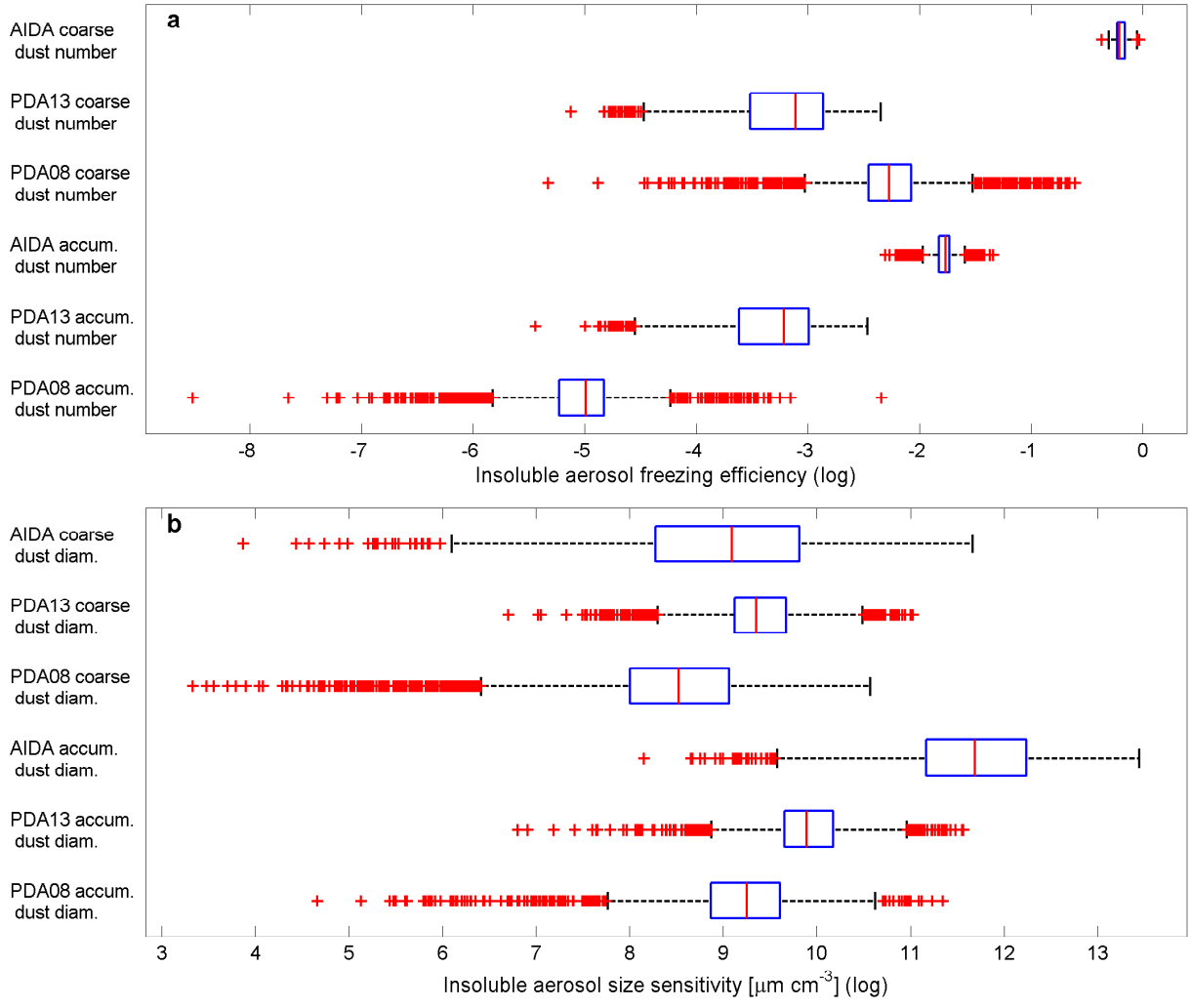

Figure 7. Log-space distributions of a random sampling of **(a)** accumulation and coarse mode dust number and **(b)** dust diameter for PDA08, PDA13, and AIDA spectra during purely heterogeneous nucleation. The box is constructed with 25th percentile, q_1; median, q_2; and 75th percentile, q_3. Outlying points are marked with crosses if they fall outside $[q_1 - 1.5(q_3 - q_1), q_3 + 1.5(q_3 - q_1)]$

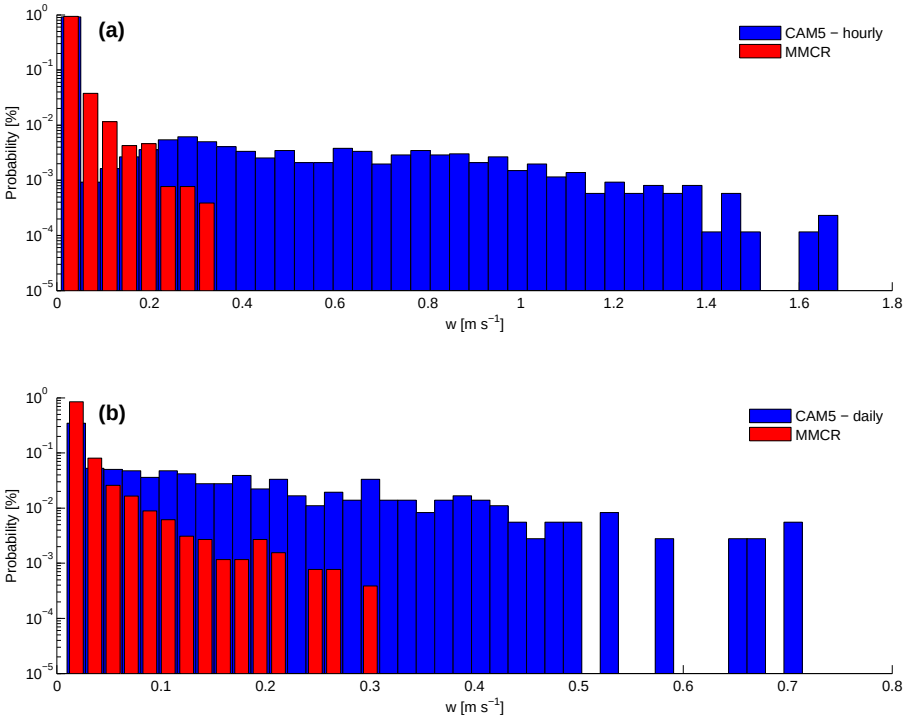

Figure 8. [SUPPLEMENTARY] Comparison of the distribution of model input updraft velocities and of millimeter cloud radar (MMCR)-measured updraft velocities after Doppler velocity decomposition. Data include all hourly-averaged values from the ARM SGP site (36.605°N, 97.485°W) throughout 1997 at the 230 ± 20 hPa pressure levels (www.arm.gov/data/pi/76). These are compared to **(a)** hourly-averaged updrafts at 232 hPa from a year-long CAM 5.1 simulation at the same latitude and longitude and **(b)** the daily-averaged updrafts over those hourly values in **(a)**. Daily-averaged values agree better with the observed updraft velocities and are used to run all simulations. A strong filter for convective towers has been applied to the data and may explain its lack of higher values.

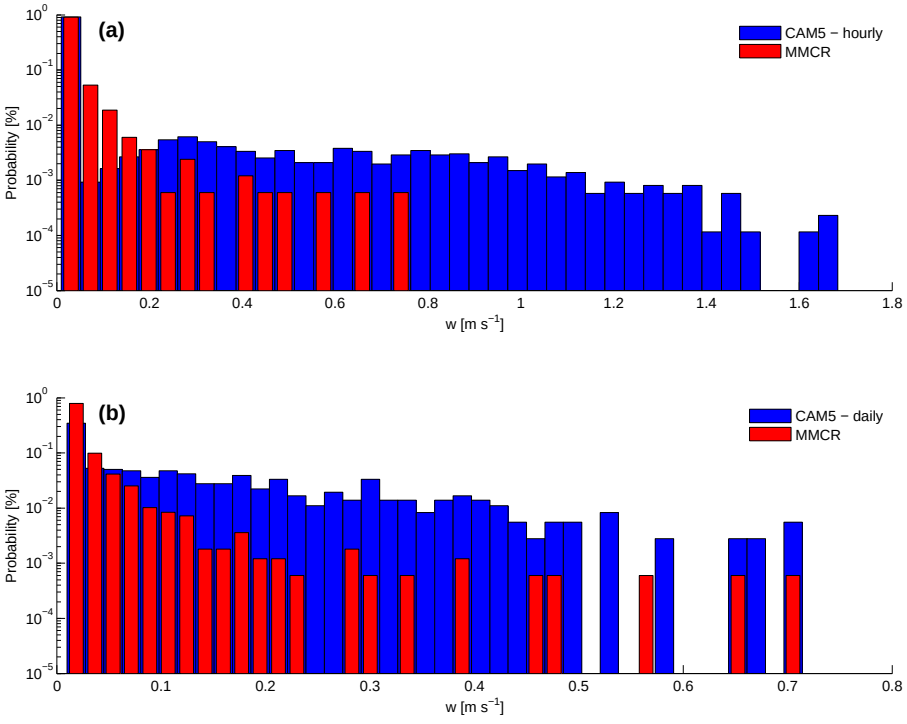

Figure 9. [SUPPLEMENTARY] Comparison of the distribution of model input updraft velocities and of millimeter cloud radar (MMCR)-measured updraft velocities after Doppler velocity decomposition. Data include all hourly-averaged values from the ARM SGP site (36.605°N, 97.485°W) throughout 2007 around the 230 ± 20 hPa pressure levels (www.arm.gov/data/pi/76). These are compared to **(a)** hourly-averaged updrafts at 232 hPa from a year-long CAM 5.1 simulation at the same latitude and longitude and **(b)** the daily-averaged updrafts over those hourly values in **(a)**. Daily-averaged values agree contain fewer instances of very large updraft and are used to run all simulations. A strong filter for convective towers has been applied to the data and may explain its lack of higher values.

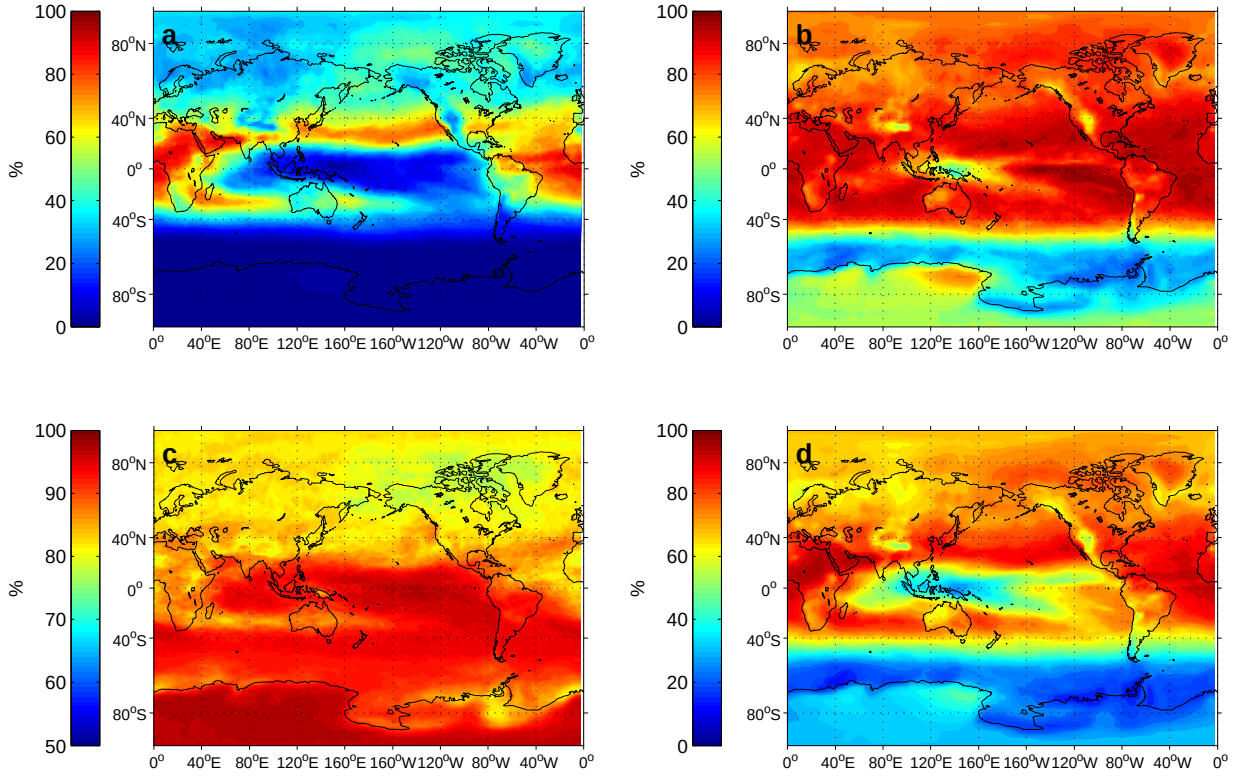

Figure 10. [SUPPLEMENTARY] Annually-averaged heterogeneously-formed fraction for all spectra. The colorbar for panel **(c)** is different than the others.

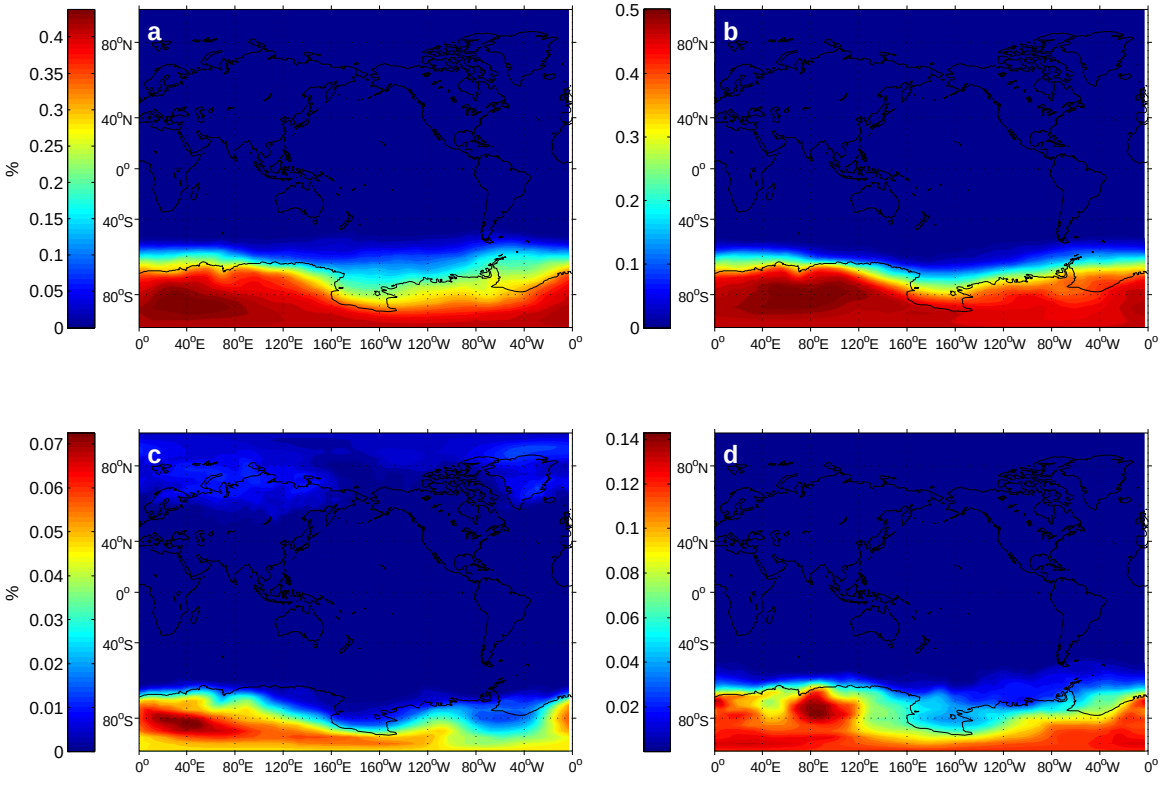

Figure 11. [SUPPLEMENTARY] Annually-averaged glassy soluble organic aerosol contribution to heterogeneously-formed crystal number in PDA13.

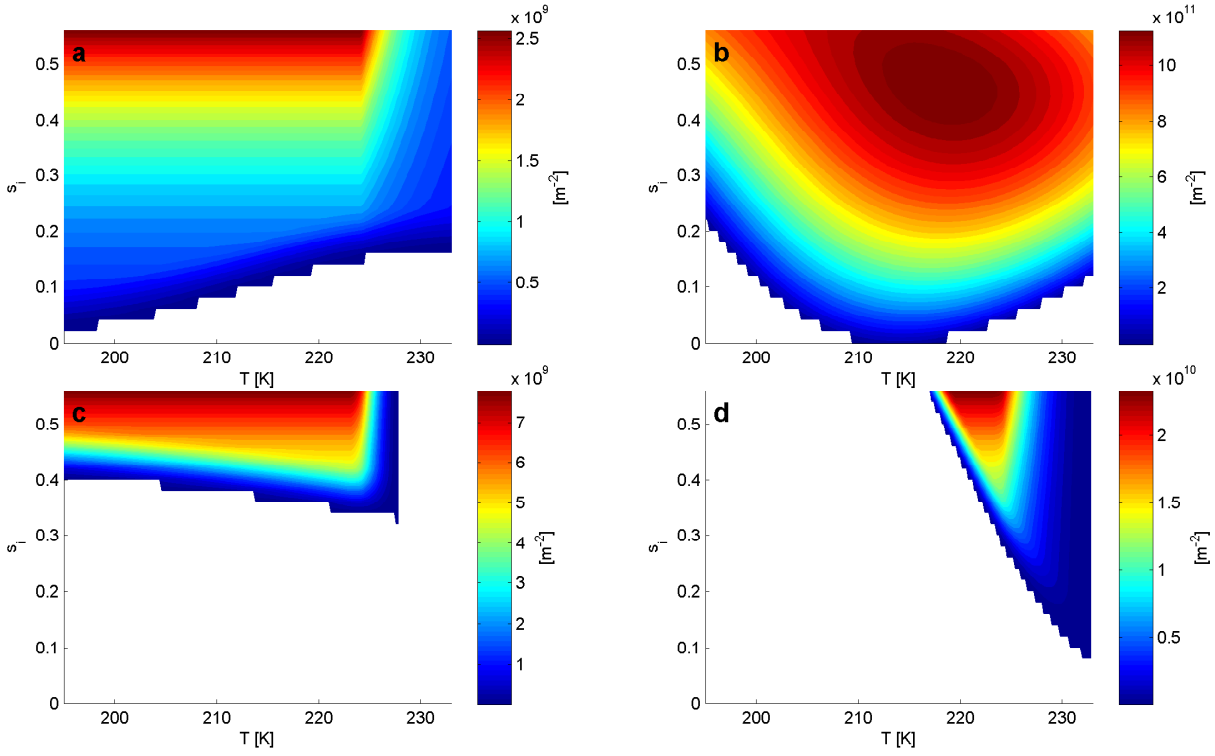

Figure 12. [SUPPLEMENTARY] Active site densities in the temperature-supersaturation space for **(a)** dust in PDA08 and PDA13, **(b)** dust in AIDA, **(c)** BC in PDA08, and **(d)** BC in PDA13.

Parameter		Value	Citation
Pressure level		232 hPa	ISCCP
Deposition coefficient	α	0.7	Skrotzki et al. 2013
Width of BC SD	σ_{BC}	1.8	Dentener et al. 2006
Width of dust SDs	σ_{DM}	1.6	d'Almeida 1987; Field et al. 2006
Width of organic SD	σ_{org}	1.8	Dentener et al. 2006
Width of sulfate SD	σ_{sulf}	2.3	Whitby 2007
Liquid mixing ratio	q_c	1×10^{-6} kgkg^{-1}	Barahona et al. 2014
Surface polarity	P_s	2	Popovicheva et al. 2007
Organic coating	F_{oc}	10%	Popovicheva et al. 2007
Threshold supersaturation for dust	$s_{i,0,DM}$	20%	Hoose and Möhler 2012
Threshold supersaturation for black	$s_{i,0,BC}$	35%	Hoose and Möhler 2012
Maximum nucleation efficiency of dust	e_{DM}	50%	Möhler et al. 2006
Effective contact angle for dust	θ_{DM}	16°	Chen et al. 2008
Maximum nucleation efficiency of black carbon	e_{BC}	2%	Pruppacher and Klett 1997
Effective contact angle for black carbon	θ_{BC}	40°	Chen et al. 2008

Table 1. Adjustable parameters for ABN15 simulations

Spectrum	INP Range [L^{-1}]	Median INP number [L^{-1}]	Interquartile range of INP number [L^{-1}]	A_{INP} range	Median A_{INP}	Interquartile range of A_{INP}
PDA08	0.047 - 5.07	0.48	1.05	0.0070 - 11.11	0.34	0.62
PDA13	0.57 - 28.6	3.60	10.56	0.67 - 49.37	10.25	10.02
CNT	6.94 - 1270.47	50.38	169.82	0.97 - 7220.64	20.80	36.52
AIDA	3.60 - 855.36	52.51	190.49	4.02 - 4549.94	20.47	24.35

Table 2. Range of predicted ice-nucleating particle numbers and abundances for different nucleation spectra